Definition and calculation of single turn coils' electrical, magnetic and electro-mechanical parameters for pulsed magnetic technologies with the finite element method and experiments

Olivier Maloberti, Omar Mansouri, Denis Jouaffre, Mohammed Hamzaoui, Jimmy Derosiere, Nicolas Buiron, Thaneshan Sapanathan, Philippe Pelca, Mohamed Rachik, Gregory Lembrouck, et al.

Definition and Calculation of Single Turn Coils' Electrical, Magnetic and Electro-Mechanical parameters for Pulsed Magnetic Technologies with the Finite Element Method and Experiments

O. MALOBERTI[1,2,*1], O. MANSOURI[1], D. JOUAFFRE[3], M. HAMZAOUI[4], J. DEROSIERE[5], N. BUIRON[6], T. SAPANATHAN[6], P. PELCA[7], M. RACHIK[6], G. LEMBROUCK[5], D. HAYE[3], J-P. LEONARD[8]

[1]*ESIEE Amiens, Ecole Supérieure des Ingénieurs en Electrotechnique et Electronique, 14 quai de la Somme, 80080 cedex 2 Amiens, France*
[2]*LPSC-UPJV, Laboratoire de Physique des Systèmes Complexes, Université Picardie Jules Verne, 33 rue Saint Leu, 80039 Amiens cedex, France*
[3]*PFT-Innovaltech, Plateforme Technologique Innovaltech, Rond-point Frédéric Joliot-Curie, 02100 Saint-Quentin, France*
[4]*LTI-UPJV, Laboratoire des Technologies Innovantes, Université de Picardie Jules Verne, INSSET 48 rue d'Ostende CS10422, 02315 St-Quentin, France*
[5]*BASIS EP, 164 rue de la Chaussée Romaine, 02100 Saint-Quentin, France*
[6]*Roberval-UTC, Laboratoire Roberval, Centre de recherche de Royallieu, Université Technologique de Compiègne, CS 60319, 60203 Compiègne, France*
[7]*Le Bronze Alloys, Etablissement de Bornel, 11 rue du Ménillet Bornel, 60540 Méru, France*
[8]*INDUXIAL, 64 Rue Hoche, 80300 Albert, France*

Keywords

Eddy currents, Lorentz force, magnetic pulse technology, numerical modelling, single-turn coil, field-shaper, skin effect.

Abstract

This paper proposes to compute the electrical behavior, including electromagnetic and electromechanical parameters, of a single-turn toroidal coil which is fed by a transient pseudo-harmonic current pulse at low or medium frequency. Solutions adapted to the specificity of the pulsed high magnetic fields technology are given, including original performance characteristics, independent on the current source, but still taking eddy currents and the skin effect into account. The finite element analysis is carried out progressively; first with time harmonics, then in the transient working condition, and finally by coupling the electromagnetic calculations to the equivalent electrical circuit of the coil. The aim of this study is to first evaluate the accuracy of a 2D axi-symmetrical numerical model by comparing it to 3D reference calculations. The reliability is valued according to measurements. The method then makes it possible to very quickly compute the main interesting coils characteristics, namely the equivalent resistance, inductance, maximum induction coefficient and finally the self and mutual force coefficients. These last new parameters are also defined in the present paper and provide important performance criteria. Finally, a sensitivity analysis will be performed to understand the impact of the main usual parameters (frequency, coil length, coil radius, airgap, electrical conductivity). The 2D model allows to save time and to build an approximate but reliable solution that might make either the transient calculation or the coupling with electrical, mechanical and thermal physics easier. After an introduction (part 2), part 3 gives the model geometry, physics and meshing. Magneto-harmonic calculations of fields and coils' parameters and a complete sensitivity analysis are performed in part 4. Transient computations are carried out on a single-turn coil made of steel without a field-shaper and are compared to experimental results in parts 5. Finally, an innovative single-turn coil with a field-shaper, both made of a non-standard copper alloy (siclanic®), has been also calculated, tested and measured in part 6. To conclude, the 2D model provides the main interesting intrinsic coil's characteristics and a fast sensitivity analysis as a function of several parameters, such as the pulse natural frequency. These parameters are needed to couple the electromagnetic process to an electrical circuit or a mechanical workpiece deformation. The present study can estimate if, in given conditions, the forming coil can ensure electromagnetic forces high enough either to initiate the process or to end it with an assembling static pressure.

*[1]: corresponding author Olivier MALOBERTI (olivie.maloberti@gmail.com, maloberti@esiee-amiens.fr)

I. NOMENCLATURE

I : total current injected in the coil

I_{peak} : peak current parameter

V : voltage at the coil terminals

$\mathbf{A}$: magnetic vector potential

$\mathbf{E}$: electric field

$\mathbf{j}$: current density

$\mathbf{H}$: magnetic field

$\mathbf{B}$: flux density or induction

$\mathbf{f}$: Lorentz force density

$\mathbf{T}$: Maxwell stress tensor

σ_m : electrical conductivity of the tube

σ_c : electrical conductivity of the coil

μ_m : magnetic permeability of the tube

ν_m : magnetic reluctivity of the tube

μ_c : magnetic permeability of the coil

ν_c : magnetic reluctivity of the coil

μ_0 : magnetic permeability of the air

ν_0 : magnetic reluctivity of the air

ω : angle velocity

f_q : frequency

δ : skin depth

P_j : copper losses

W_m : magnetic energy

R : total equivalent resistance

L : total equivalent inductance

B_{max} : maximum induction generated in the airgap

K_b : maximum induction coefficient

F_c : maximum force density in the coil

F_m : maximum force density in the tube

K_c : self-force coefficient

K_m : mutual-force coefficient

R_{mi} : internal radius of the tube

R_{me} : external radius of the tube

e_p : thickness of the tube

g : airgap between the tube and the coil

R_{ci} : internal radius of the coil

R_{ce} : external radius of the coil

L_{fi} : internal radius of the field-shaper

L_{fe} : external radius of the field-shaper

L_{ci} : internal radius of the coil

L_{ce} : external radius of the coil

II. Introduction and State of The Art

Production of high static magnetic fields can be obtained with superconducting materials. Pulsed magnetic fields can be created either with consumable or permanent coils. This paper investigates the design of single-turn coils made of bulk conducting materials, without self-destruction. Different geometries of such inductors are studied to generate pulsed high magnetic fields. Gersdorf & al. (1965) [1] introduced the design of high field magnet coils for electromagnetic pulses, Wilson & al. (1965) [2] proposed the design of efficient field-shapers next to the coils to control the high field area. Psyk et al. (2011) [3] made a review of such inductors used in pulsed magnetic technologies, especially the electromagnetic forming process. He introduced several practical cases for which the single-turn coil (see **Figure 1**) is often preferable to the multi-turn coil because it is simpler and more robust. Single turn coils and field-shapers studied and proposed by previous authors are thus used in pulsed magnetic and electromagnetic forming technologies.

The coil and field-shaper should be made of a high conducting material with a high mechanical resistance and durable either. Nowadays, the most used materials for the single-turn coils are steel alloys, CuZr alloys (Copper Zirconium) for multi-turn coils and CuBe alloys (Copper Beryllium) for single-turn coils and the field-shapers. Steel alloys are not very good electrical conductors and therefore copper alloys are sometimes preferred (Arnaud & al., 1985) [4]. CuZr alloys are not resistant enough and cannot be used for coils without reinforcements. CuZr and especially CuBe alloys are expensive and contains dangerous elements: Zirconium is toxic and Beryllium is toxic and carcinogenic. Research is taking place in order to use other copper alloys to replace steels, CuZr and in particular the CuBe alloy for single-turn coils and field-shapers. Experiments have been carried out using non-standard alloys with copper, nickel and silicium (siclanic® alloy) or copper and cobalt (cuprofor® alloy). Another goal of this work is to estimate accurately the current's distribution that may cause a heating process located in the skin depth and the magnetic pressure and force that may cause small damaging deformations on the surface of the tool.

Following the state of the art and future needs listed by El-Azab & al. (2003) [5], we suggest computing, testing and measuring single-turn coils, made of a massive coil, an optional field-shaper and an internal conducting tube. The first coil will be made of steel and the second coil and field-shaper will be made of a new and non-standard copper alloy (siclanic®). Due to a cut within the coil and field-shaper, it is strictly speaking a 3D component with no axial symmetry, as this is shown in reference Bartels & al. (2009) [6]. In fact, several authors have already studied this kind of magneto-forming coil with the help of the 3D Finite Element Method. Conraux & al. (2006) [7] began to develop and use 3D numerical models based on the Finite Element Method for the Electro-Magnetic Forming process simulation and improvements. These kind of 3D models also presented by Robin & al. (2008) [8] are extremely time consuming but sometimes necessary when speaking about complex 3D geometries and extreme values located at the edges or near the cut, as it is explained by Bahmani & al. (2009) [9]. It is therefore interesting to find another method, that would be accurate enough to give approximately the same nominal results as the ones obtained by the 3D numerical models, whilst being much faster. This new method could be very attractive for several purposes: 1) the multi-physics simulation that requires too much memory and time in 3D; 2) the transient non-linear simulation with electrical and mechanical couplings that takes up less time and memory space in 2D as proposed by Pasca and Fireteanu (2004) [10] for a multi-turn coil for example; 3) the optimal sizing of the pulsed inductor by giving the corresponding sensitivity analysis for important parameters. Heuzé & al. (2013) in [11] considers the use of Proper Generalized Decomposition methods dedicated to the coil optimization but only with parallel 2D numerical simulations on a multi-turn coil example. Because the cut within the coil or the field-shaper is very small,

we would like to investigate the possibility to reduce the single-turn coil geometry into an equivalent 2D axi-symmetrical model, but still producing a very good estimate of the true magnetic field, current density and Lorentz force, as explained by Maloberti & al. (2015) [12]. Deng & al. (2007) in [13] carried out 2D simulations of the magneto-forming process including an attractive force with a flat coil and an expanding axial coil. Guglielmetti (2012) in [14] studied the electromagnetic and mechanical behaviour of a cylindrical multi-turn coil and a tube with a 2D numerical method. Since the coil is highly conducting and the generator creates a current pulse that varies very quickly in time (from 10 to 100 kHz) (Yanuka & al., 2016) [15], we suggest computing the model for both harmonic and transient states to analyze the eddy currents, skin effects and induced Lorentz forces in the single-turn coil. Some authors performed analytical calculations of the magnetic field and the self and mutual inductances for similar cylindrical coils. Dodd (1967) in [16] provided the foundations for such electromagnetic induction problems. Dodd and Deeds (1968) in [17] carried out investigations on the good basis functions to be used, *i.e.* the modified Bessel functions for quasi-static induction problems. Figueiredo and Laks (1989) in [18] introduced the use of the Kelvin functions for similar magnetic cylinders. Conway (2001) in [19] found the exact solution for the magnetic field in axi-symmetrical solenoids, but providing that the current source distribution is known and simple. Labinac et al. (2006) in [20] calculated the magnetic fields of cylindrical coils due to a known surface current and a volume current in a cylindrical coil. Yu and Han (1987) in [21] calculated the quasi-static self-inductance of air core circular coils with a rectangular cross section. Conway (2007) in [22] gave the calculation for non-axial coils. Ravaud et al. (2010) in [23] added the calculation of the mutual inductance and the force exerted between thick coils carrying uniform current volume densities. Most of these authors performed their calculations in quasi-static working conditions and with known current sources, *i.e.* without eddy currents, or for currents in a direction different from the orthoradial direction and for magnetic materials. In this study, we are looking for accurate solutions adapted to the the pulsed high magnetic fields technology and we introduce original definitions of induction and force coefficients as relevant performance characteristics, independent on the current source in the orthoradial direction. To do so, we must take into consideration eddy currents and skin effects inside conducting materials. In fact, the magnetic pulse technology contains bulk coils, sometimes with a secondary coil called the field-shaper and another secondary or tertiary coil which a conducting tube can be. These secondary and tertiary coils are not connected to a known current source, the eddy current is rather induced by the primary coil. In this paper, the 2D Finite Element Method allows an accurate calculation of fields and performance characteristics in the whole parts and a fast method for a complete sensitivity analysis as a function of various sizing parameters.

III. 3D MODEL AND 2D APPROXIMATION

We propose to analyze a 3D toroidal single-turn coil with a cut and feeding terminals by using the Finite Element Method (FEM). Some foundations of the numerical computation for similar induction problems can be found in Diellabi and Latreche (2014) [24] with the same software. Analytical and experimental validations on the magnetic field and inductance calculations are proposed by Kennedy & al. (2011) [25] for the induction heating process. Due to two symmetries ((x,y) is a π+ symmetry plane and (y,z) is a π- symmetry plane), the problem can be reduced to ¼ but stays 3D (see **Figure 1**). From now, we will assume that the thickness of the cut is small enough to admit an axi-symmetry around the (oz) axis. Using the cylindrical coordinates (r,θ,z), there is an invariability *versus* the coordinate θ. The model reduction in 2D will have to be compared to the exact 3D solution given by Maloberti & al. (2015) [12]. It will then be possible to investigate analytical solutions initiated in Mansouri & al. (2016) [26]. A future study will propose analytical models dedicated to the design and optimization of single-turn coils for the magneto-forming process and will use reference calculations and sensitivity analysis given by the present numerical models.

The geometry is defined thanks to the following parameters: the internal R_{ci}, intermediate R_{cie} and external R_{ce} radius of the toroidal coil, and its useful (L_{ci} or L_{fi}) and total (L_{ce} or L_{fe}) length (see **TABLE 1** in the Appendix A.1). This coil, fed by a current

pulse, will generate a time varying magnetic field inside the coil and so eddy currents will be induced in conducting parts. The tube has got a thickness $e_p=R_{me}-R_{mi}$ and the air gap between the coil and the tube is $g=g_{mc}$. There is sometimes an intermediate field-shaper between the coil and the tube. This secondary coil is also a toroidal part with a cut. Its role is to adapt any coil to several tubes by concentrating the field in the useful area.

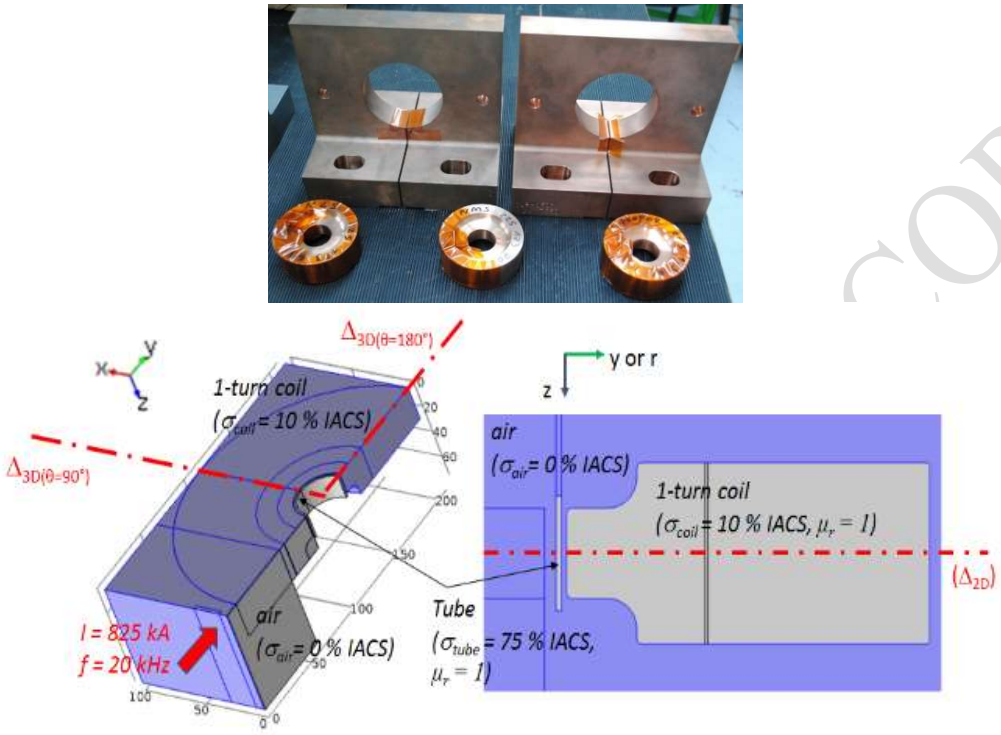

Figure 1. 3D geometry and its 2D reduced model.

The coil and/or field shaper are made of a steel alloy (electrical conductivity σ_c and permeability $\mu_c=\mu_0$) and are surrounded by the air ($\sigma_a=0$ and $\mu_a=\mu_0$). The internal tube is made of a copper alloy (conductivity σ_m and permeability $\mu_m=\mu_0$). (see **TABLE 2**).

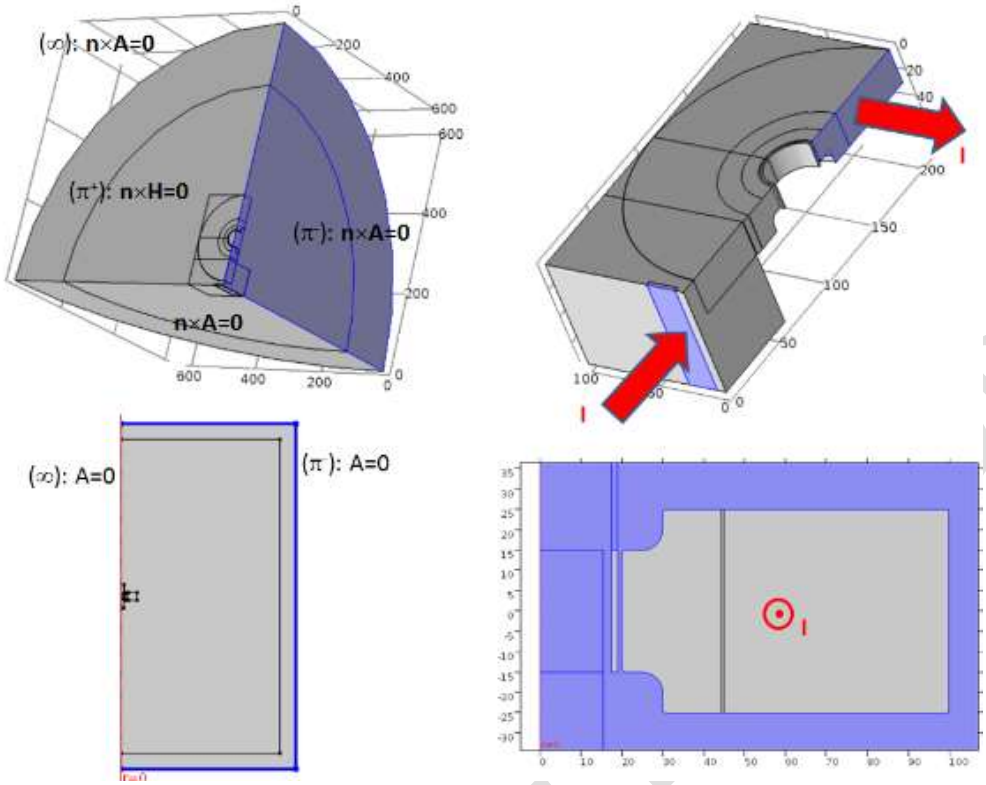

Figure 2. Constraints and Boundary conditions.

We assume that neither the magnetic flux nor the electric current are generated outside the infinite limit (1). Due to the π^- symmetry, no magnetic flux can circulate through the (y,z) plane, and due to the π^+ symmetry, no electrical current can circulate through the (x,y) plane (1). The magnetic field **H** and flux density **B** are consequently inside the (y,z) plane and perpendicular to the (x,y) plane. No electric current (**j**) can go through the air and a total current $I(t)=Iexp(i\omega t)$ is imposed, feeding the coil (with $\omega=2\pi f_q$ as the angle velocity and f_q as the frequency) through the terminal (2). The two degrees of freedom, the magnetic vector potential **A** and the electric scalar potential V, linked to the magnetic and electric fields **H** and **E** respectively, are set to zero at the initial stage. All of this results in the following limit constraints (see **Figure 2**).

$$\begin{aligned}(\infty)&: \mathbf{n}\cdot\mathbf{B}=0 \Leftrightarrow \mathbf{n}\times\mathbf{A}=\mathbf{0}\\ (\pi^-)&: \mathbf{n}\cdot\mathbf{B}=0 \Leftrightarrow \mathbf{n}\times\mathbf{A}=\mathbf{0}\\ (\pi^+)&: \mathbf{n}\cdot\mathbf{j}=0 \Leftrightarrow \mathbf{n}\times\mathbf{H}=\mathbf{0}\end{aligned} \quad (1)$$

$$I=\iint_{coil}\mathbf{j}\cdot\mathbf{d}^2\mathbf{x}=\iint_{coil}\left(\mathbf{j}_s-\sigma\partial_t\mathbf{A}\right)\cdot\mathbf{d}^2\mathbf{x} \quad (2)$$

The mesh of **Figure 3** is adapted to the skin effect thanks to a skin depth that depends on the permeability μ ($\mu=\nu^{-1}$, ν is the reluctivity), the conductivity σ and the angular velocity $\omega=2\pi f_q$ (f_q is the frequency) (3). The mesh size d at the facing interfaces is chosen inferior to one third of the skin depth δ.

$$\delta=\sqrt{\frac{2\nu}{\sigma\omega}}=\sqrt{\frac{\nu}{\sigma\pi f_q}} \quad (3)$$

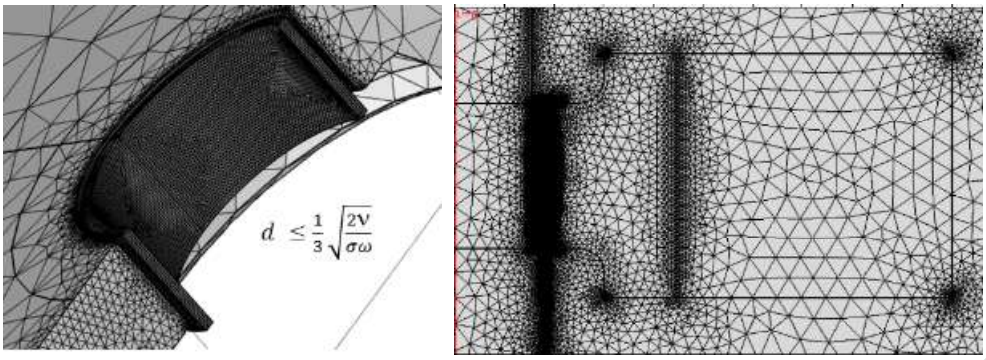

Figure 3. Mesh (3D 1,400,000 elements and more than 1 day computation time; 2D 50,000 elements at maximum and less than 1 min. computation time).

IV. Magneto-Harmonic Computations

A. Governing equations

The model is computed first with the magnetic field formulation in the harmonic working condition. The use of the magnetic vector potential **A** automatically satisfies the magnetic flux conservation principle and the Maxwell Faraday laws. The current conservation principle and Maxwell Ampere law result in the equation (4), similar to that of a diffusion equation:

$$\nabla \times \left(\nu \nabla \times \mathbf{A}\right) + j\sigma\omega\mathbf{A} = \mathbf{j_s} \tag{4}$$

$\mathbf{j_s}$ is the current source density. σ is the electrical conductivity (σ_c = 10% IACS, σ_m = 75% IACS, σ_a = 0). ν is the magnetic reluctivity ($\nu = \mu^{-1} = \nu_0 = \mu_0^{-1}\ (1/(4\pi)).10^7\ H^{-1}m$, ∇ is the "Nabla" operator).

B. Local computation results

Next, we focus on local fields: the magnetic vector potential A, the flux density B, the current density j and the Lorentz force density f, as a function of the radial position r along the lines (Δ_{2D}) and (Δ_{3D}) (5). The total current magnitude I equals 825 kA, with no phase shift and with the frequency f_q= 20 kHz. All the fields can be deduced from **A**.

$$\begin{cases} \mathbf{B} = \nabla \times \mathbf{A} \\ \mathbf{j} = \nabla \times \left(\nu \mathbf{B}\right) = -j\sigma\omega\mathbf{A} \\ \mathbf{f} = \mathbf{j} \times \mathbf{B} \end{cases} \tag{5}$$

In **Figure 4**, **Figure 5**, **Figure 6** and **Figure 7**, we analyze the field and density results as a function of the radial coordinate r.

The potential **A** on the (Δ_{2D}) and (Δ_{3D}) lines is along the x or θ direction: $\mathbf{A} = A\mathbf{u}_\theta$. In **Figure 4**, we observe at first that the real part of the potential is almost linear and the imaginary part is nil in the free internal space of the coil without any tube. However, this is no longer the case inside the coil material due to the magnetic field damping effect. When the tube is introduced, the damping effect remains inside both the coil and the tube materials. The magnetic potential slope in the free space inside the tube is much lower than the one in between the coil and the tube. The main variations and imaginary parts are in the conducting regions.

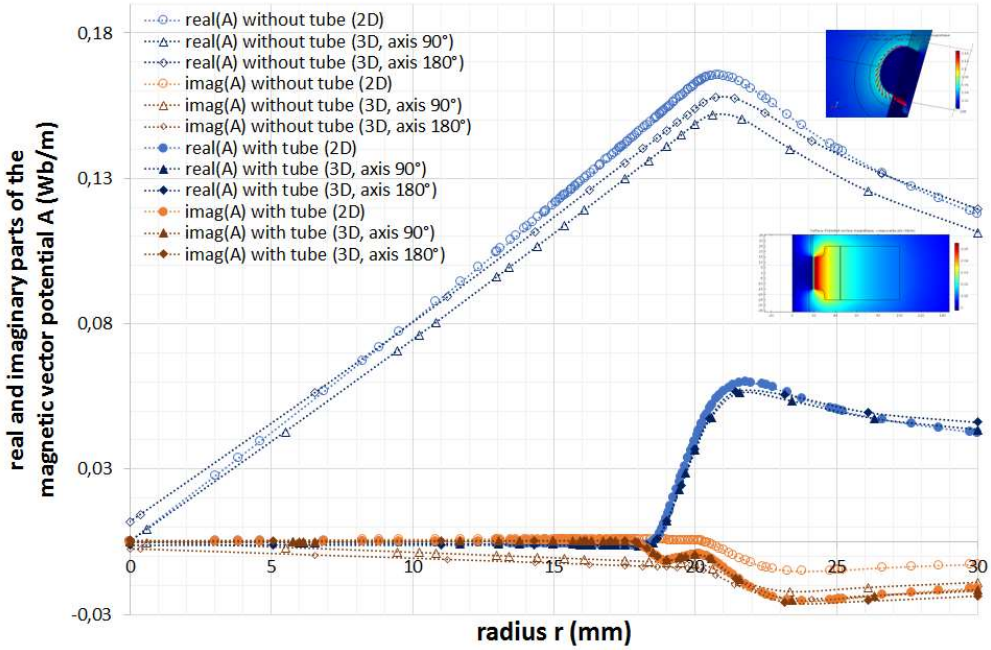

Figure 4. Magnetic vector potential A.

The flux density **B** on the (Δ_{2D}) and (Δ_{3D}) lines is along the z direction: $\mathbf{B} = B\mathbf{u}_z$. In **Figure 5**, we see that induction magnitude |B| is almost constant in the free internal space of the coil without any tube, but< is rapidly decreasing inside the coil due to the skin depth. When the tube is introduced, the skin effect remains in the coil and the tube, each with its skin depth (δ_c = 1.50 mm in the coil and δ_m = 0.53 mm in the tube). No flux is generated in the free space inside the tube such that the induction magnitude, two times higher than without the tube, is focused in the gap between the coil and the tube.

The current density **j** is along the x or θ direction: $\mathbf{j} = j\mathbf{u}_\theta$. In the **Figure 6**, no current can go in the air region. The current density magnitude |**j**| is at its maximum on the conductors' skin and is rapidly decreasing inside both the coil and the tube skin depth. The current magnitude in the coil with the tube is two times higher than without the tube. This implies eddy currents are induced in the coil with an additional phase angle. Mainly due to the higher electrical conductivity of the tube, the current density (only eddy currents) is three times higher in the tube than in the coil.

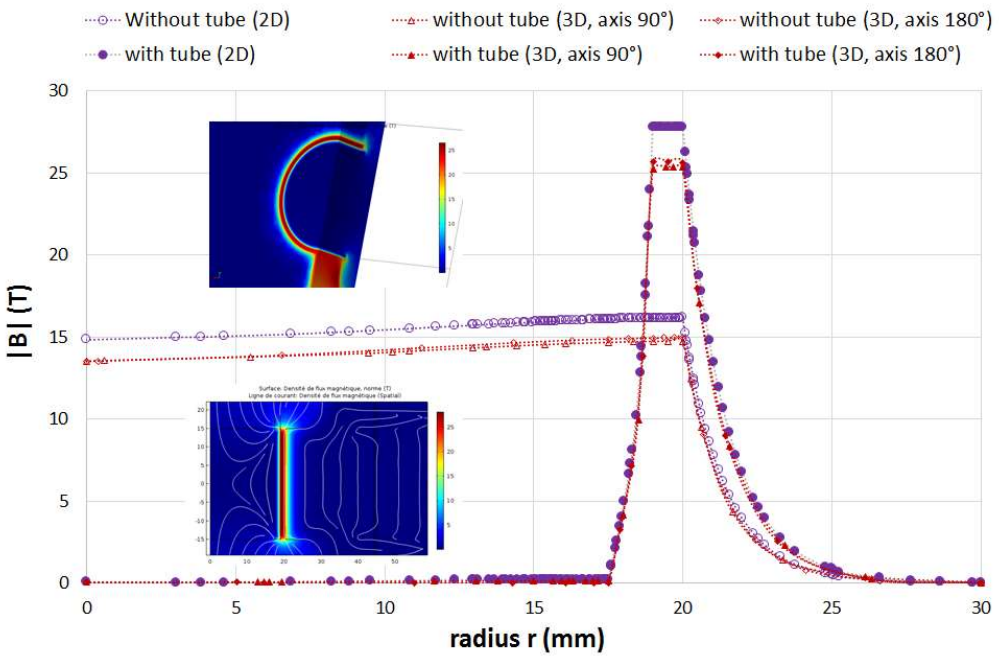

Figure 5. Magnetic flux density B.

By using the flux **B** and current **j** densities, the Lorentz force density **f** is computed by using either the cross product (7) or the divergence of the Maxwell stress tensor **T** (6).

$$T_{ij} = \nu_0 \left(B_i B_j - \frac{1}{2} |B|^2 \delta_{ij} \right) \tag{6}$$

$$\mathbf{f} = \mathbf{j} \times \mathbf{B} = \nabla \cdot \mathbf{T} \tag{7}$$

The Lorentz force density **f** on the (Δ_{2D}) and (Δ_{3D}) lines is necessary along the y or r direction: $\mathbf{f} = f\mathbf{u}_r$. In **Figure 7**, no force acts on the air region. The force is always negative inside the tube, tending to compress it; and it is always positive inside the coil, tending to expand it. The force density **f** is proportional to the cross product between **j** and **B** and therefore behaves similarly to **j** and **B** in inside the conducting materials, with a corresponding half skin depth.

Finally, we notice in **Figure 4**, **Figure 5**, **Figure 6** and **Figure 7** that an agreement is found for all the results on A, |B|, |j| and |f| between the 2D and the 3D computations with a reasonable discrepancy smaller than 4% inside the conducting materials and 12% inside the air. This error is mainly due to the slot in the coil base, separating the two voltage terminals.

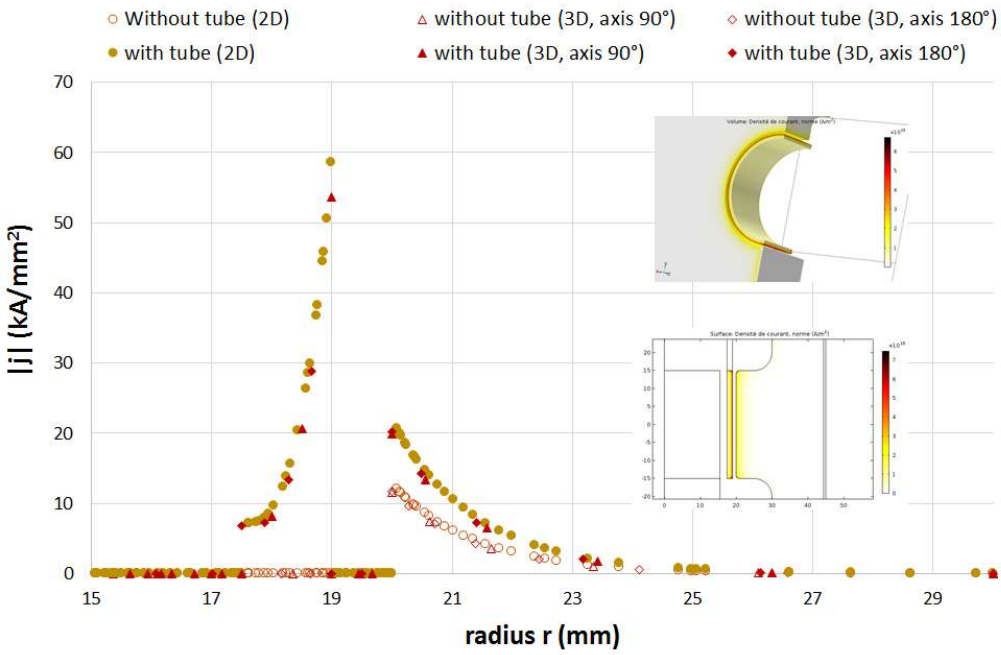

Figure 6. Electrical current density j.

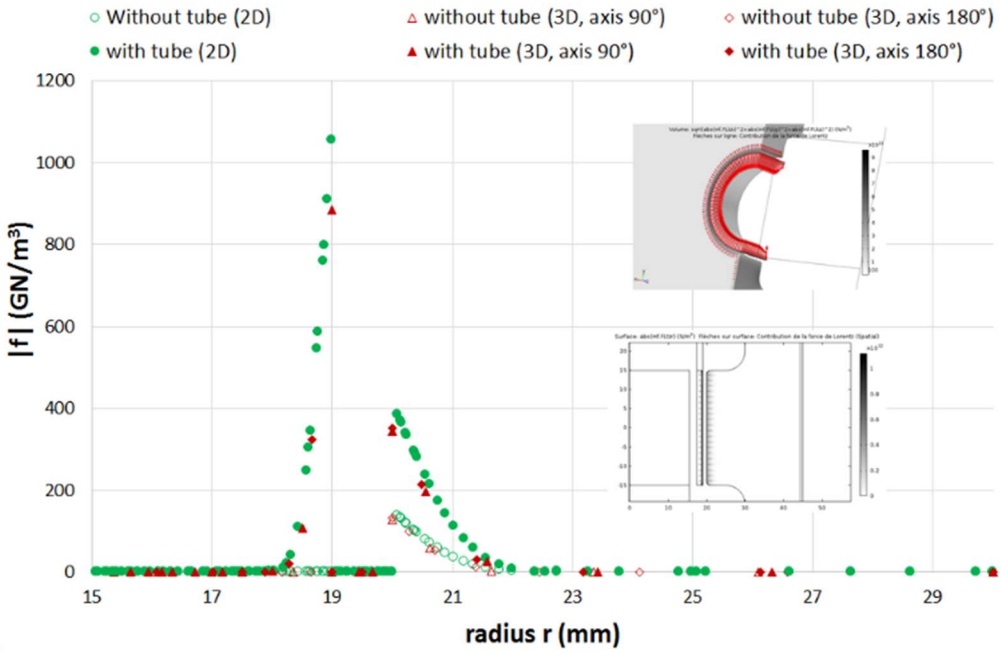

Figure 7. Lorentz force density f.

C. Global computation results

Now, we compute the resistive Joule losses P_j (8) and the stored magnetic energy W_m (9).

$$P_j = \iiint_{space} \frac{|\mathbf{j}|^2}{2\sigma} d^3x \Rightarrow R = \frac{2P_j}{I^2} \tag{8}$$

$$W_m = \iiint_{space} \frac{|\mathbf{B}|^2}{2\mu} d^3x \Rightarrow L = \frac{2W_m}{I^2} \tag{9}$$

Explanations for the inductances' calculation can be found in reference Ghali and Rahman (2009) [27]. If the problem is linear

with constant properties σ and μ, these integrals lead to the coil resistance R and inductance L, similar to that of Babic and Akyel (2000) [28]. The latter gave the self and mutual inductances of thin wall solenoids and disk coils. The results given in the present paper do not make any assumption on either the current source distribution or the eddy currents density. On one side, the skin effect is computed but on the other side, no separation can be found between the self and the mutual inductances. L represents the total equivalent inductance of the coil, including mutual effects due to eddy currents in conducting regions. In **Figure 8** and **Figure 9**, we draw the curves of R and L as a function of f_q. L comes from the magnetic energy. The higher the frequency, the lower the coils surface and the inductance. The tube is behaving like a secondary coil in short circuit with a mutual inductance that must be subtracted from the self-inductance. As a result, the total equivalent inductance L with a tube is lower. R comes from the Joule losses with dependence on the coil circumference and skin depth. The higher the frequency the smaller the skin depth and the conductance G=1/R. The tube introduces an additional resistance. As a result, the total resistance R with a tube is higher.

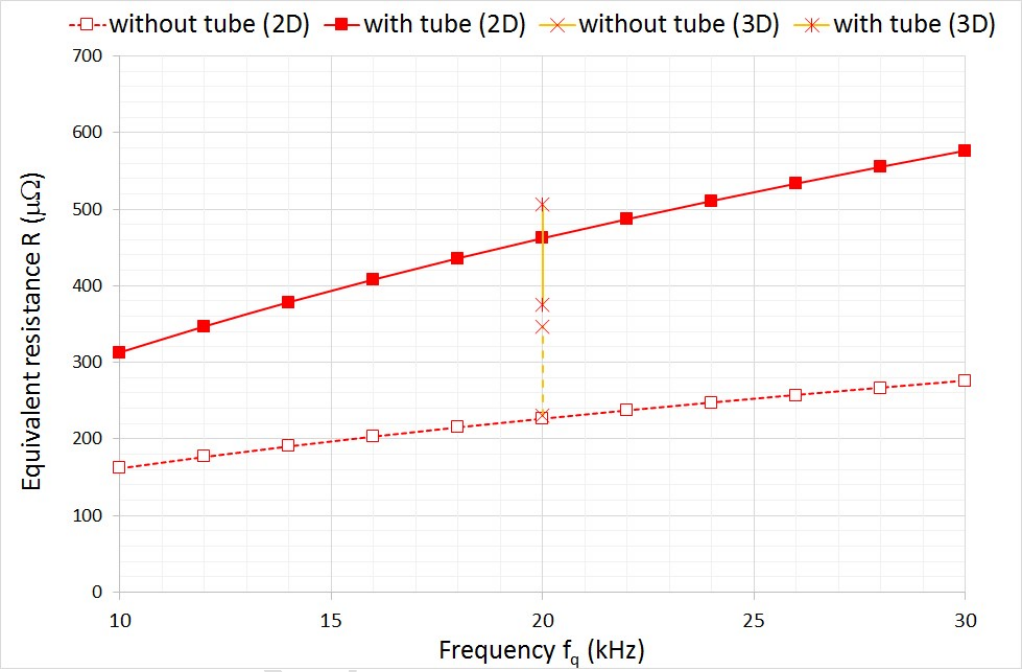

Figure 8. Equivalent coil resistance R.

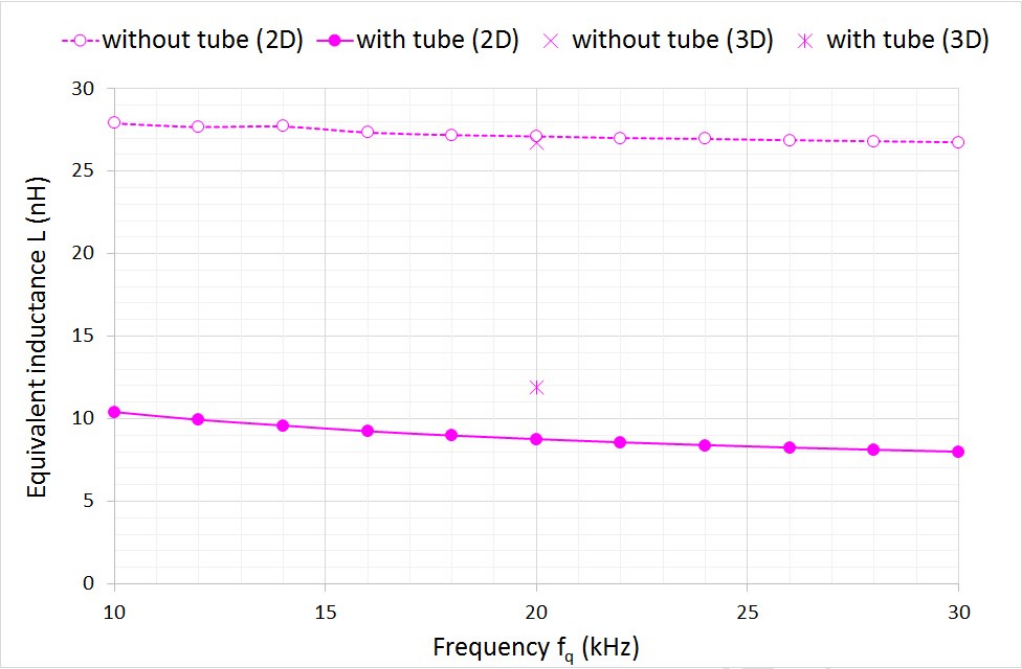

Figure 9. Equivalent coil inductance L.

Then, we can look at the maximum magnetic flux density B_{max} generated at the coil internal surface (10) and the tube external surface (10) respectively.

$$B_{max} = \max_{airgap}\{\mathbf{B}\cdot\mathbf{u}_z\} = \max_{tube}\{\mathbf{B}\cdot\mathbf{u}_z\} = \max_{coil}\{\mathbf{B}\cdot\mathbf{u}_z\} \tag{10}$$

The maximum flux density coefficient K_b (11) defined by the ratio between $\mathbf{B_{max}}$, also called the magnetic induction, and the current per unit length ($Z=L_{ci}$) must also be analysed. The physical unit of K_b is given by the absolute magnetic permeability μ in [$H.m^{-1}$]. In a way, it represents the coil's ability or easiness to focus a high magnetic field inside the airgap.

$$\mathbf{K_b} = \frac{\mathbf{B_{max}}}{\mathbf{(I/Z)}} = \frac{\mathbf{max_{airgap}\{B.u_z\}}}{\mathbf{(I/Z)}} \tag{11}$$

In **Figure 10**, we draw the curves of the induction coefficient K_b as a function of f_q both with and without a tube. It is higher with a tube due to field sources in two regions instead of one.

Finally, we can look at the maximum force density F_c and F_m acting on the coil (12) and the tube (13) skin respectively.

$$F_c = \max_{coil}\{\mathbf{f}\cdot\mathbf{u}_r\} \tag{12}$$

$$F_m = \max_{tube}\{\mathbf{f}\cdot\mathbf{u}_r\} \tag{13}$$

Now let's look at the self and mutual force density coefficients K_c (14) and K_m (15) defined by the ratio between the maximum force density and the squared current per unit length multiplied by the squared root frequency. In fact, it can be shown, partially by Mansouri & al. (2016) [26], that the Lorentz force, as the cross product of the current and flux densities, is in a first approximation proportional to $(\mu/\delta)(I/Z)^2$. The physical unit of the force coefficients is thus given by the product $(\sigma^{1/2}\mu^{3/2})$.

$$K_c = \frac{F_c}{\sqrt{\omega}\left(I/Z\right)^2} = \frac{\max_{coil}\{\mathbf{f}\cdot\mathbf{u}_r\}}{\sqrt{\omega}\left(I/Z\right)^2} \tag{14}$$

$$K_m = \frac{F_m}{\sqrt{\omega}\left(I/Z\right)^2} = \frac{\max_{tube}\{\mathbf{f}\cdot\mathbf{u}_r\}}{\sqrt{\omega}\left(I/Z\right)^2} \quad (15)$$

In **Figure 11**, we draw the curves of the self and mutual force density coefficients K_c and K_m respectively as a function of the frequency f_q with and without a tube to deform (maximum force density magnitude created in the coil itself and in the tube respectively, per squared root Hertz and per squared Ampere per unit length). These coefficients are loosely dependent on f_q. They can thus be considered as performance parameters for the coil with or without the tube regardless of the source. $K_m/K_c \propto (\sigma_m/\sigma_c)^{1/2}$ and K_c is higher with the tube due to force balance effects.

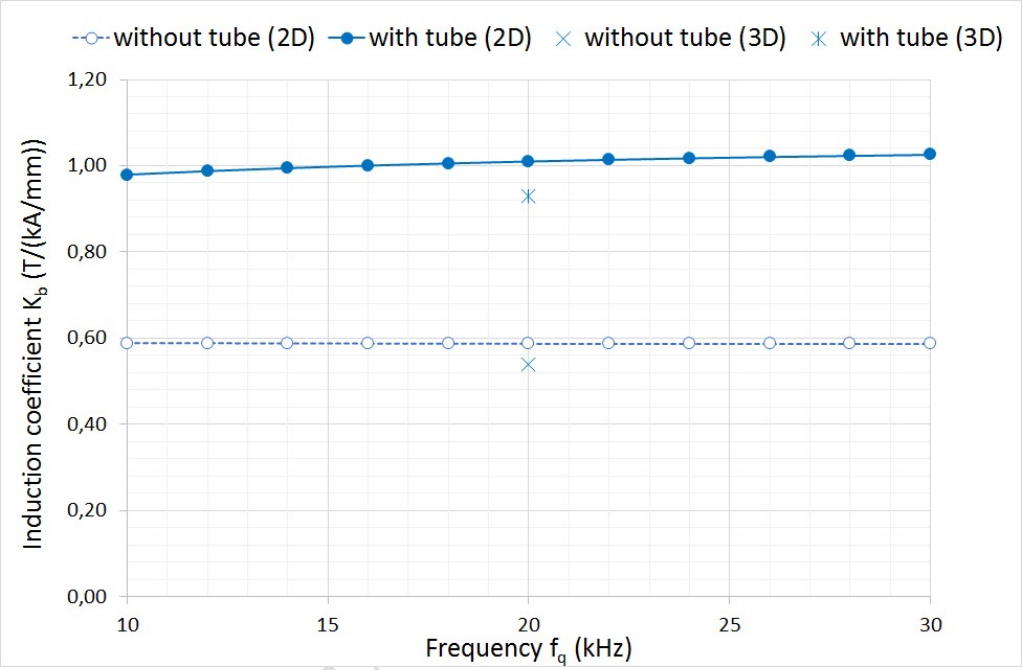

Figure 10. Maximum induction coefficient K_b.

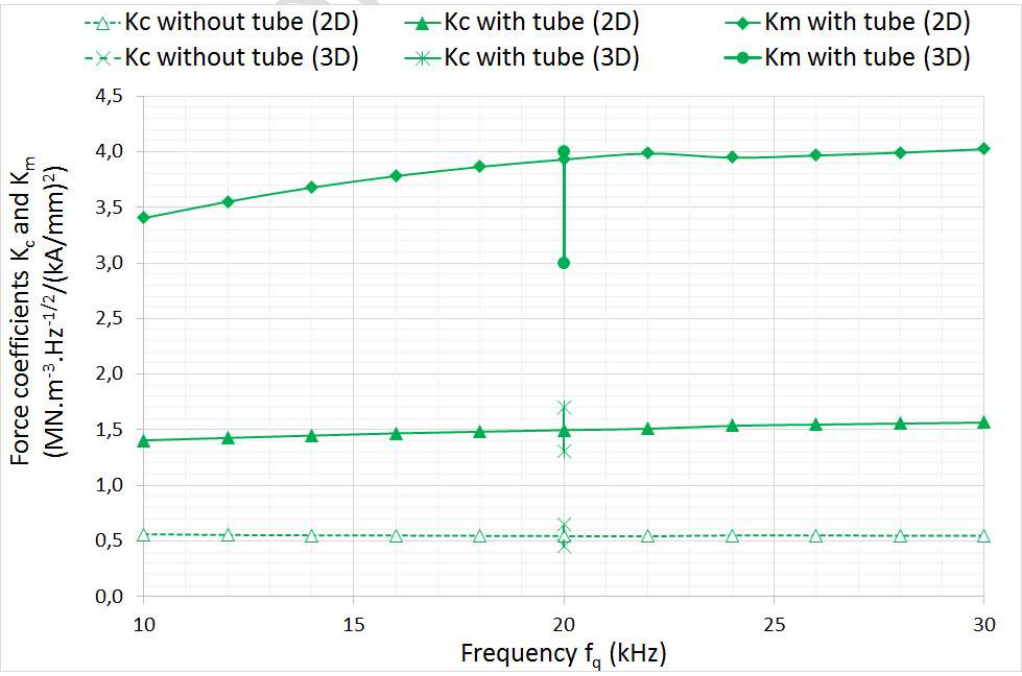

Figure 11. Equivalent force density coefficients K_c and K_m.

3D results show some inaccuracies because we decided to compute two extreme values for R, L, K_b, K_c and K_m. The first extreme

values correspond to the one obtained without the coil connection terminals. The second extreme values are obtained with the coil connection terminals. Despite these uncertainties, similarities are always found between 3D and 2D models. Of course, these similarities are reached only for the nominal values of the induction, current density and force density, namely the average values obtained on the axis (Δ_{2D}), and between axis ($\Delta_{3D(\theta=90°)}$) and ($\Delta_{3D(\theta=180°)}$). These last values called nominal values, are the most useful for the sought deformation of the tube. It does not take into consideration the extreme values near the cut or the edges of the coil or the field-shaper, that can be accurately determined only by 3D simulations (Bahmani & al., 2009) [9].

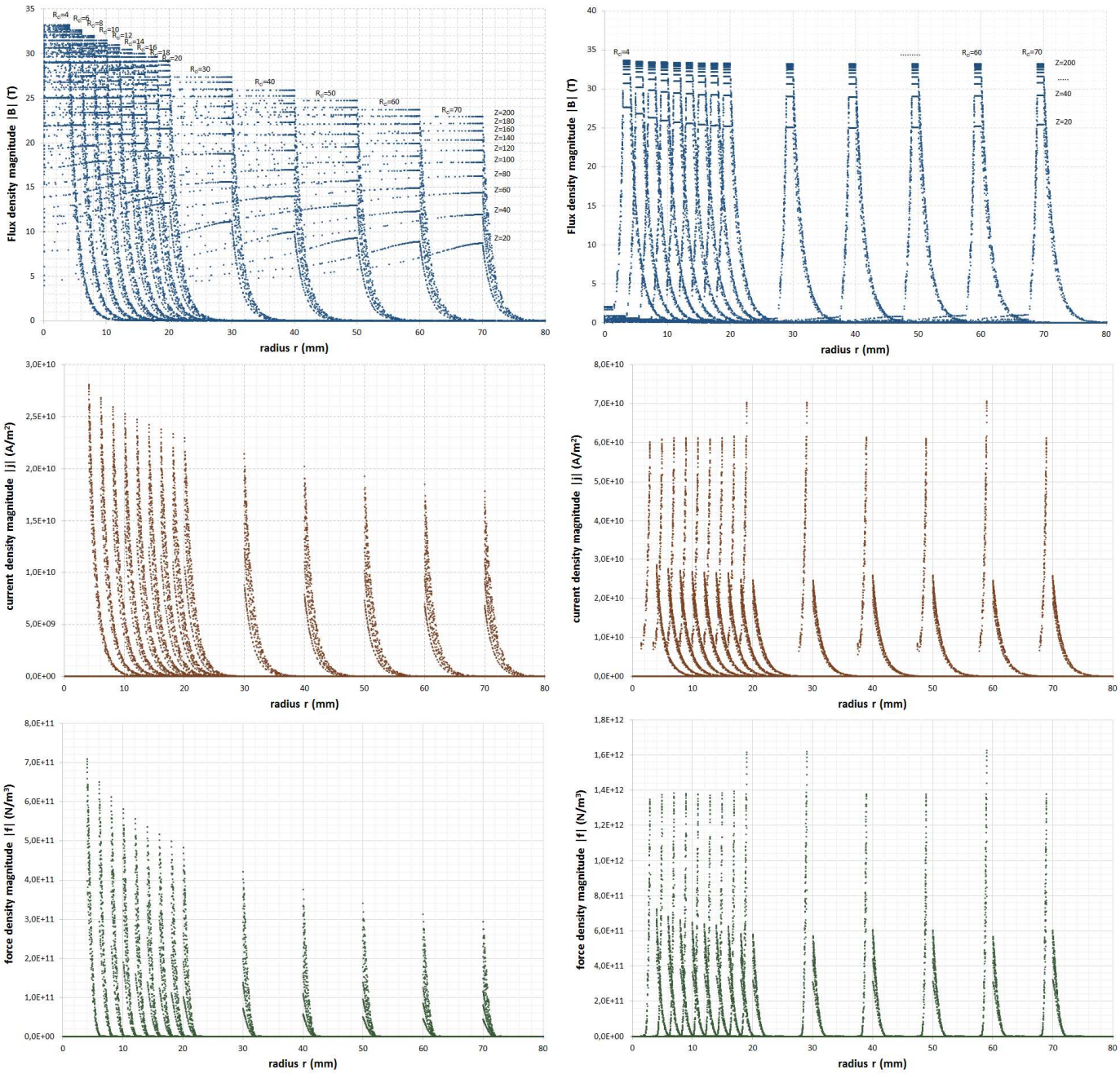

Figure 12. Computing results on B, j and f as a function of the radius r for several values of the geometrical parameters R_{ci}=[4,6,8,10,12,14,16,18,20,30,40,50,60,70] (internal useful radius of the coil) and Z=[20:20:200] (useful length of the coil along direction z)

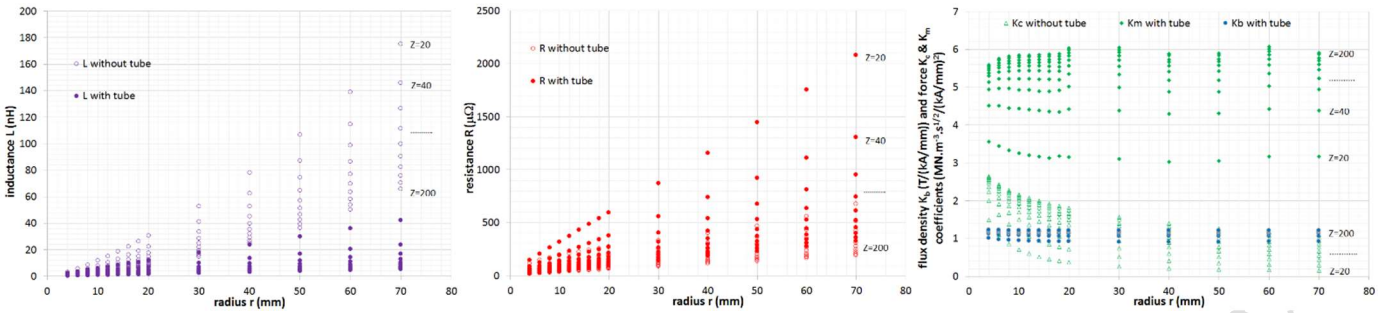

Figure 13. Sensitivity analysis of resistance R, inductance L, induction and force coefficients K_b, K_c & K_m as a function of R_{ci} and Z.

D. Sensitivity analysis on main parameters

One of the main advantages of the reduced 2D models is to speed up the calculations, particularly in a sensitivity analysis when there are a lot of calculations to do. We first propose to analyze the sensitivity of results to R_{ci} (coil internal radius) and Z (the coil length). The fields and densities are shown in **Figure 12**. The coil parameters are given in **Figure 13**. Logically, the coil inductance L and resistance R increase with R_{ci} (flux section and current path) and decrease with Z (flux path and current section). Despite a constant current per unit length (I/Z) and a constant frequency f_q (20 kHz), K_b and K_m decrease with the ratio R_{ci}/Z. However, they tend towards a constant limit when there is a large enough length Z such that (R_{ci}/Z) becomes smaller and smaller.

We then propose to analyze the variation of results with regard to the airgap g (gap between the coil and the tube) and σ (the coil σ_c or tube σ_m conductivity). The fields and densities are shown in **Figure 14** (g), **Figure 15** (σ_c) and **Figure 16** (σ_m). The coil parameters are given in **Figure 14** (g) and **Figure 17** (σ_c and σ_m). Due to a bigger volume of air, the inductance L increases with the airgap g. However, due to a decreasing interaction between the coil and the tube, the resistance R and force coefficients K_c and K_m will decrease with g. The electrical conductivity mainly impacts the skin depth ($\propto 1/\sqrt{\sigma}$) and current magnitude ($\propto\sigma$) in the corresponding conducting region. As a result, R gradually decreases with $\sqrt{\sigma}$, the force of the corresponding region is largely enforced with $\sqrt{\sigma}$, and the force of the other region stays approximately constant. To a lesser extent, the inductance L is also weakened by the increase in conductivity because of a decreasing skin depth and flux section.

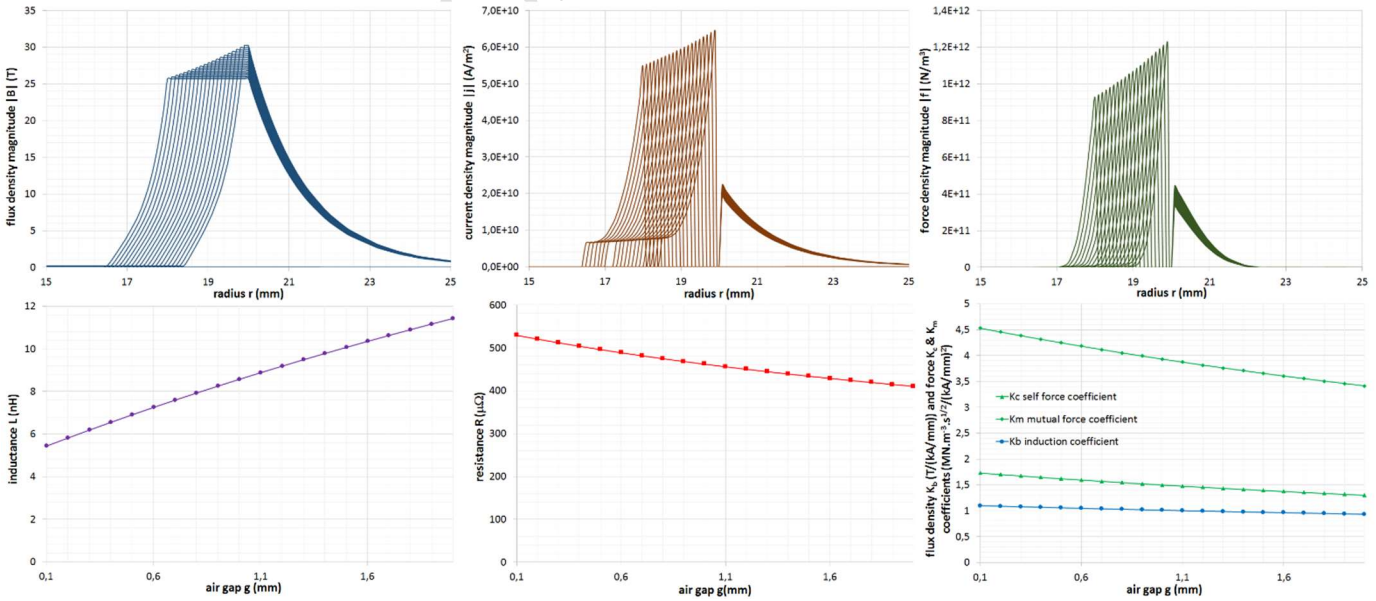

Figure 14. Sensitivity analysis on local and global results as a function of the air-gap g between the coil and the tube.

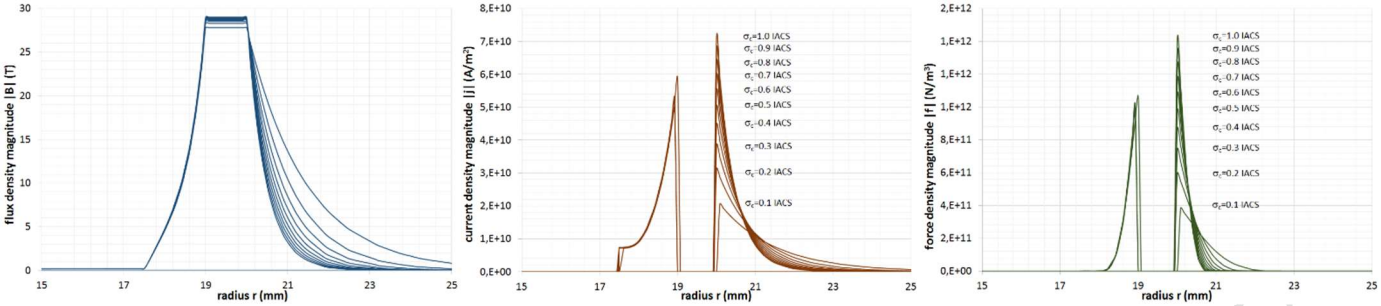

Figure 15. Sensitivity analysis on local results as a function of the coil conductivity (σ_c).

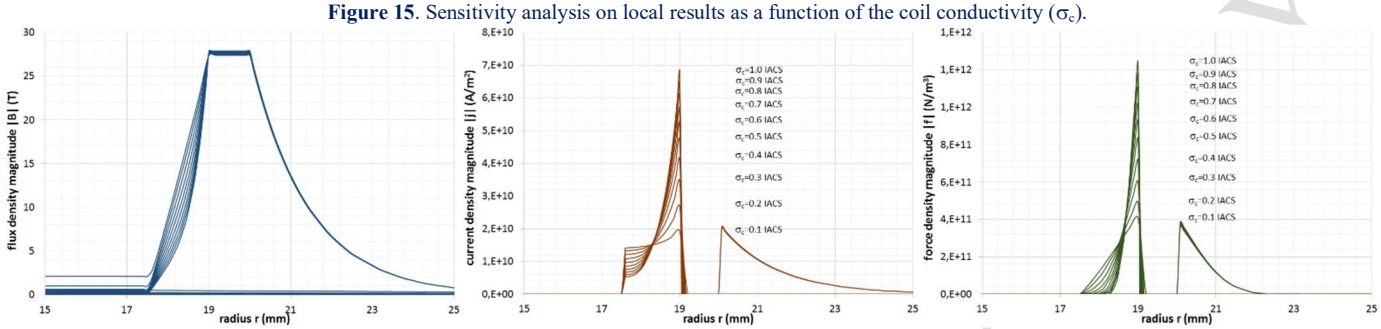

Figure 16. Sensitivity analysis on local results as a function of the tube conductivity (σ_m).

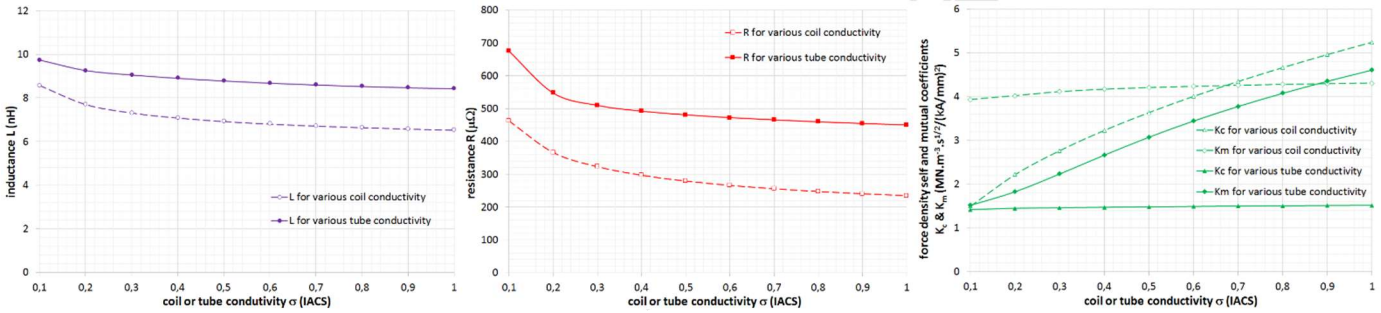

Figure 17. Sensitivity analysis on local and global results as a function of the coil and tube conductivity (σ_c and σ_m).

V. Transient Magnetic Computations

A. *Governing equations*

The model can be computed with the magnetic field formulation in the transient working condition. The use of the magnetic vector potential **A**(t) still automatically obeys the magnetic flux conservation principle and the Maxwell Faraday laws. The current conservation principle and Maxwell Ampere law result in a diffusion like partial differential equation (16):

$$\nabla \times \left(\nu \nabla \times \mathbf{A}\right) + \sigma \partial_t \mathbf{A} = \mathbf{j_s} \tag{16}$$

(σ_c = 7% IACS, σ_m = 30% IACS, σ_a = 0, $\nu = \mu^{-1} = \nu_0 = \mu_0^{-1}$).

B. *Test-Case studied – **first experiment***

We finally investigate two industrial cases. The first prototype is a 1-turn massive coil made of steel without a field-shaper, studied first with no tube deformation. The geometry and the materials are defined in the Appendix A.2 with normalized values, due to a non-disclosure agreement. The coil is connected to a pulse generator made of a capacitor with cables. The measurement procedure provides the current I(t) generated inside the coil and the voltage V(t) appearing at its terminals. We propose to use the current pulse measured as an input for the simulation, with an exponentially decaying harmonic function (17) (**Figure 23**).

$$I(t) = I_{peak} \exp\left(-\frac{t}{\tau}\right)\sin\left(2\pi f_q t\right) \tag{17}$$

I_{peak} is the current peak parameter, $\tau=2(L+L_1)/(R+R_1)$ is the time decay constant and $f_q = \sqrt{(1/((L+L_1)C)-(1/\tau)^2)}$ is the natural resonant frequency of the system.

*C. Local computation results – **first experiment***

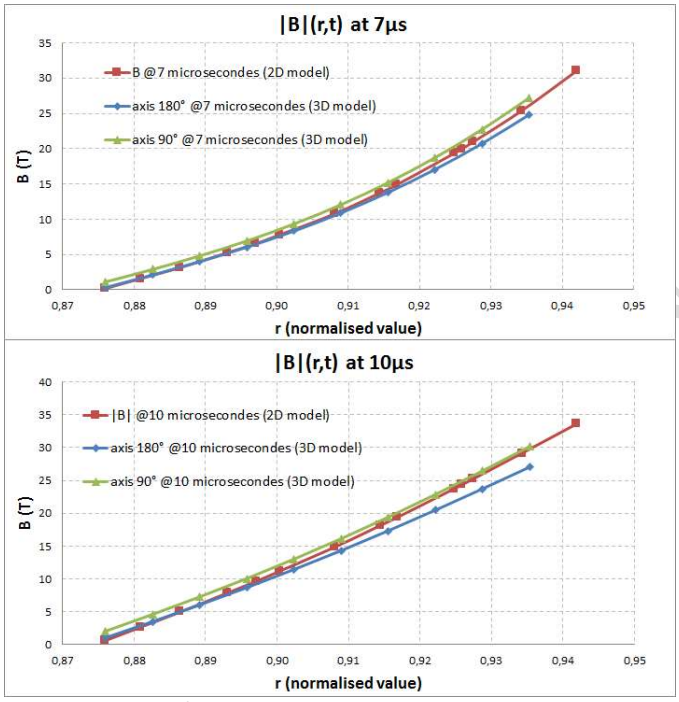

Figure 18. Transient local flux density in experiment 1.

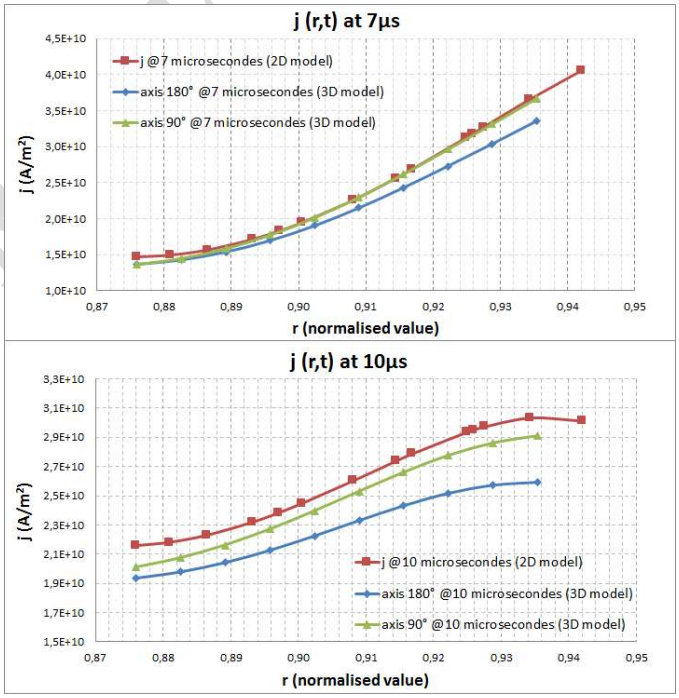

Figure 19. Transient local current density in experiment 1.

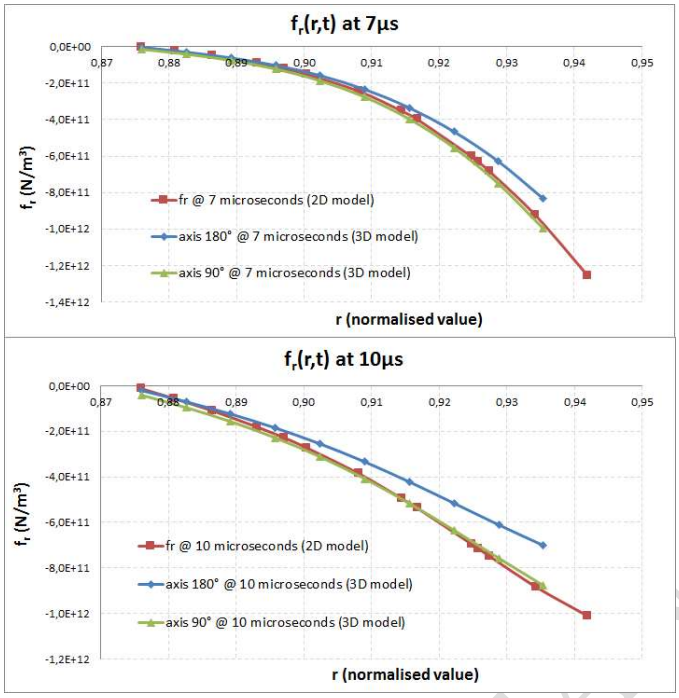

Figure 20. Transient local force density in experiment 1.

Next, we will focus on local fields: the flux density B(r,t), the current density j(r,t) and the force density f(r,t) respectively, as functions of the radius r along the lines (Δ_{2D}), ($\Delta_{3D(\theta=90°)}$) and ($\Delta_{3D(\theta=180°)}$) (5) and for 2 time steps (times 7 and 10 µs). The generator has 5 banks with capacitors charged at the voltage V_0 = 8000 V. The current I is given by (17) with a current peak parameter I_{peak} = 774 kA, a time constant τ = 50 µs, a natural frequency f_q = 22 kHz (with a tube, σ_l = *30 % IACS*) and with no phase angle.

The times 7 µs and 10 µs have been chosen in accordance to the peak value achieved by the Joule power losses or the force and the magnetic field or the current, as can be seen in **Figure 18**, **Figure 19** and **Figure 20**. The aim of this computation step is to estimate the discrepancies between the 2D and the 3D models. These discrepancies always stay below 10%.

*D. Global computation results – **first experiment***

We will focus on global features as a function of time: The Joule losses $P_j(t)$, the magnetic power $P_b(t)$, the total power absorbed P(t) and the surface force density on the coil $F_c(t)$ and on the tube $F_m(t)$. The generator has only one capacitor bank charged at the highest voltage (V_0 = 8000 V). The current I equals (17) with a current peak parameter I_{peak}=175.6 kA (with a tube) and 165.7 kA (without a tube), a time constant τ=41.7 µs (with a tube) and 43.5 µs (without a tube), with no phase angle and a natural frequency f_q = 27.5 kHz (with a tube) and 27 kHz (without a tube).

As can be seen in **Figure 21**, the Joule loss is oscillating but as an active power, and always stays positive with a maximum value around 7 µs. It represents the loss induced by the current of the source and eddy currents in the conducting regions. The magnetic power corresponds to the time derivative of the magnetic energy stored by the inductor, mainly in the air. It is oscillating and as a reactive power can be either positive or negative.

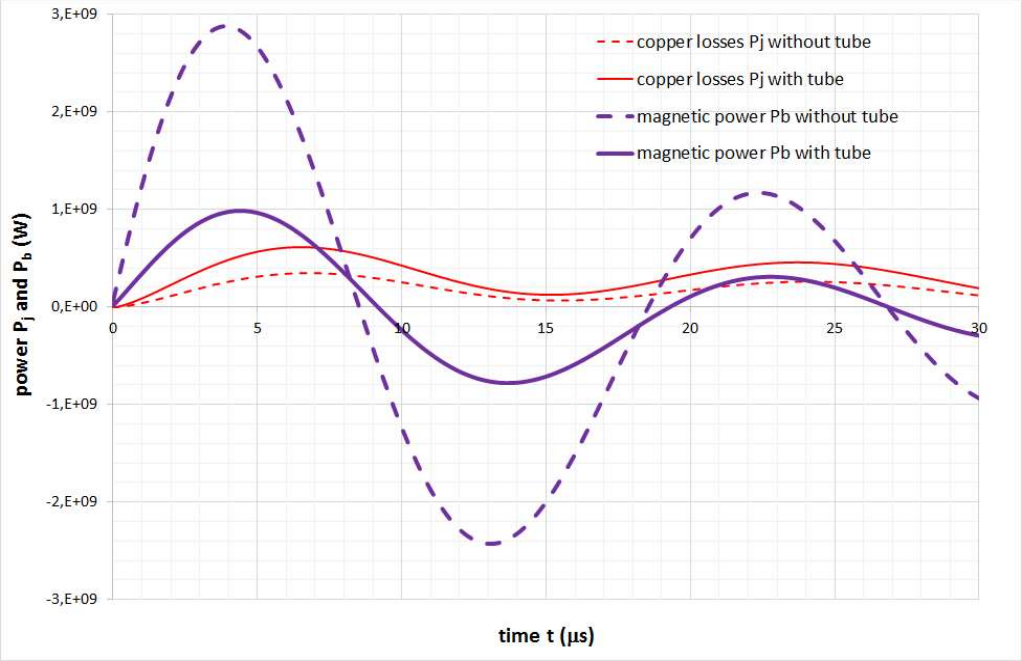

Figure 21. Transient copper losses and magnetic power.

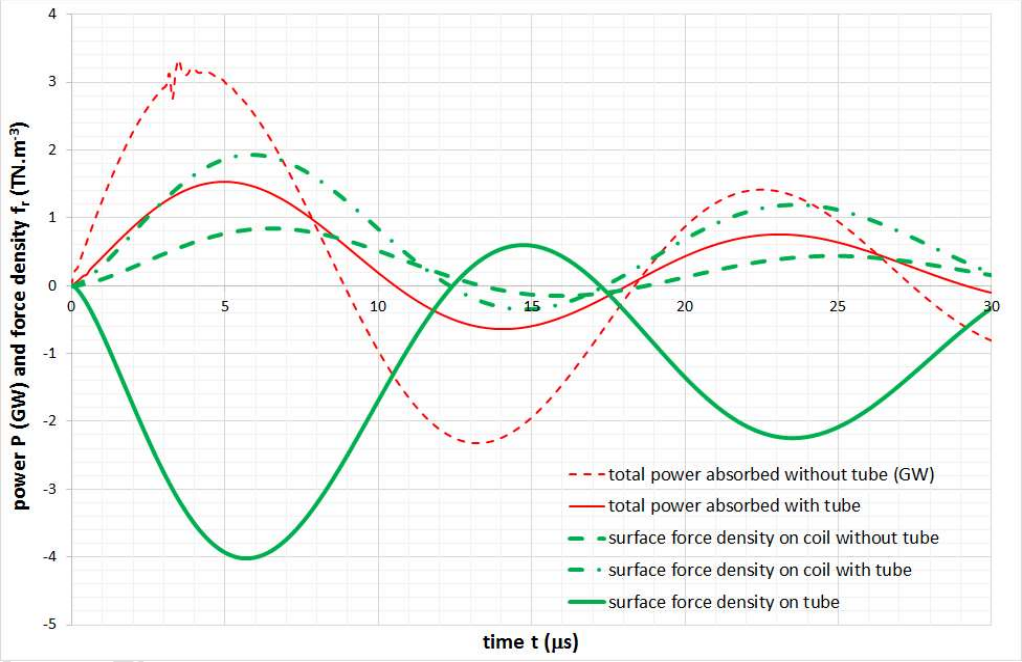

Figure 22. Transient total power and surface force density.

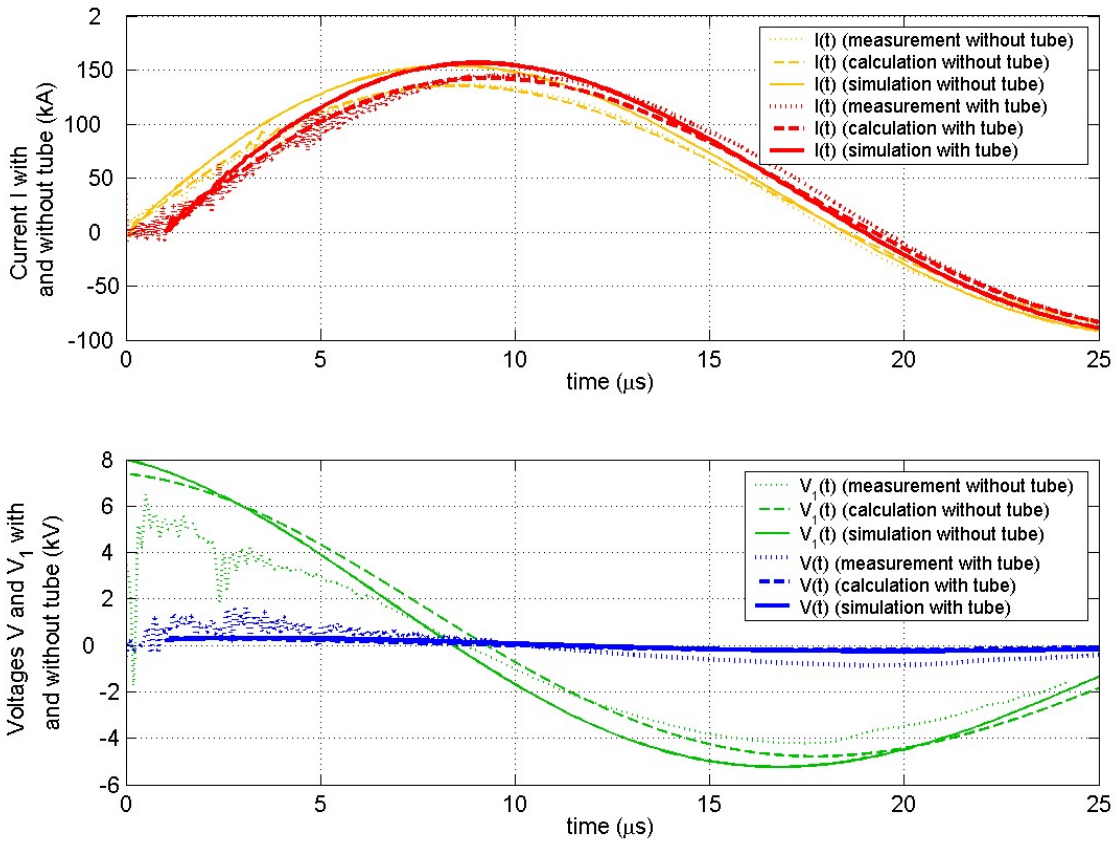

Figure 23. Transient current I and voltage V_1 or V pulses computed and measured in the first experiment (steel coil without field-shaper, without or with a tube). Only the first pulse, the most important, is shown.

In **Figure 22**, the total power absorbed by the coil must equal the sum of the Joule losses and the magnetic power. Because the magnetic power is much greater than the Joule losses, the total power is varying in a very similar way to the magnetic power. Keeping the same initial voltage V_0, the power without a tube is bigger than the one with a tube, because the impedance with a tube is smaller than without a tube. The induced force density either in the coil or in the tube is behaving similarly to the Joule losses, causing the coil to expand (positive average force) and the tube to compress (negative average force).

*E. Experimental results – **first experiment***

Even if it is not possible to measure the force density and to check previous results on the maximum force and the force acting onto the surface of the coil and the tube, it is possible to measure the transient current inside the coil and the transient voltage at its terminals. These have been measured, recorded, filtered and shown in **Figure 23**. The total current I equals (17) with a peak current I_{peak}=175.6 kA (with a tube) and 165.7 kA (without a tube), a time constant of τ=41.7 µs (with a tube) and 43.5 µs (without a tube), with no phase angle and a natural frequency f_q = 27.5 kHz (with a tube) and 27 kHz (without a tube).

F. Discussion

As shown in **Figure 23**, the model allows an accurate computation of the same pulses for sufficiently high voltage but neglects high frequency disturbances mainly due to the spark gaps between the generator and the inductor. Finally, it has to be mentioned that despite the usual magnetic properties of steel, high energy measurements with enormous peak currents will induce a magnetic saturation. As a result, the apparent equivalent permeability of steel in this case is very close to that of air. The steel is considered as a non-magnetic material like most conducting materials usually used in such an application.

VI. Electrical Circuit Coupling

A. *Electrical circuit and governing equations*

The model can still be computed with the magnetic field formulation in the transient working condition. The use of the potential **A**(t) still satisfies the flux conservation principle and the Maxwell-Faraday law. The current conservation principle and Maxwell Ampere law lead to the equation (18):

$$\nabla \times \left(\nu \nabla \times \mathbf{A}\right) + \sigma \partial_t \mathbf{A} = -\sigma r^{-1} \partial_\theta V \tag{18}$$

The voltage gradient $r^{-1}\partial_\theta V$ is calculated thanks to a coupled simple equivalent electrical circuit proposed in **Figure 24**. Once the capacitor C of the generator is charged at a given voltage V_0, a switch is closed to let a current pulse circulate towards the inductor in cables of equivalent resistance R_1 and inductance L_1.

B. *Test-Case studied – **second experiment***

The second inductor prototype is a 1-turn coil equipped with a field-shaper (bulk ring with a cut) both made of a non-standard copper alloy. Arnaud et al. (1985) in [4] studied the electrical and mechanical properties of standard copper alloys. Lockyer and Noble (1999) in [29] proposed some fatigue mechanisms inside similar copper alloys (CuNiSi). Two new materials called the Siclanic® and Cuprofor® materials (@ Le Bronze Alloys) can been used in the present coil as they have a known electrical conductivity but no complete mechanical characterisations yet. The input variables such as the geometry and the material properties are defined in the Appendix A.3 and normalized due to a non-disclosure agreement. The wish to design a new coil with non-usual materials leads us to perform several computations to calculate its performance and the maximum force it must withstand. The coil is connected to a pulse generator made of a capacitor with cables. In this section, we propose to compute the current pulse I(t) measured by using the initial voltage $V_0=V_1(t=0)$ as an input for the simulation and coupling the electromagnetic model and the equivalent electrical circuit. The transient current's characteristics such as the peak current I_{peak}, the time constant τ, and the natural frequency f_q are thus not assumed but calculated. First, the aim is to analyze the quality of 2D electromagnetic and electrical results, leaving out the mechanical coupling. The generator is limited to one capacitors bank charged at various voltages (V_0 = 2500, 3500, 4500, 5500, 7500 V) to avoid any plastic deformation of the tube.

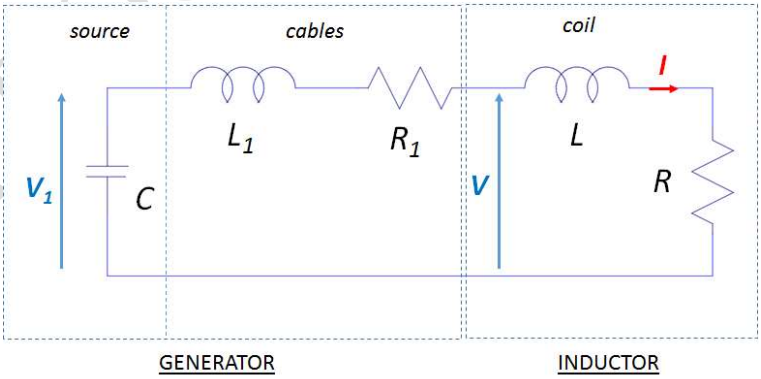

Figure 24. Equivalent electrical circuit of magnetic pulse system.

C. *Local computation results – **second experiment***

The **Figure 25** shows the 3D and 2D computations of the local radial force density $f(r,t)=f_r(r,t)$ inside the tube as a function of the radial position r along the lines (Δ_{2D}) and ($\Delta_{3D(\theta=180°)}$) and for four important time steps (2, 6, 10 and 18 µs). Both the peak and mean value of the force and its transient behavior can be correctly estimated with either the 2D or the 3D models. We do however notice a 2 µs delay between the two models, which may not be critical in the current-voltage, force density and potential mechanical

deformation predictions.

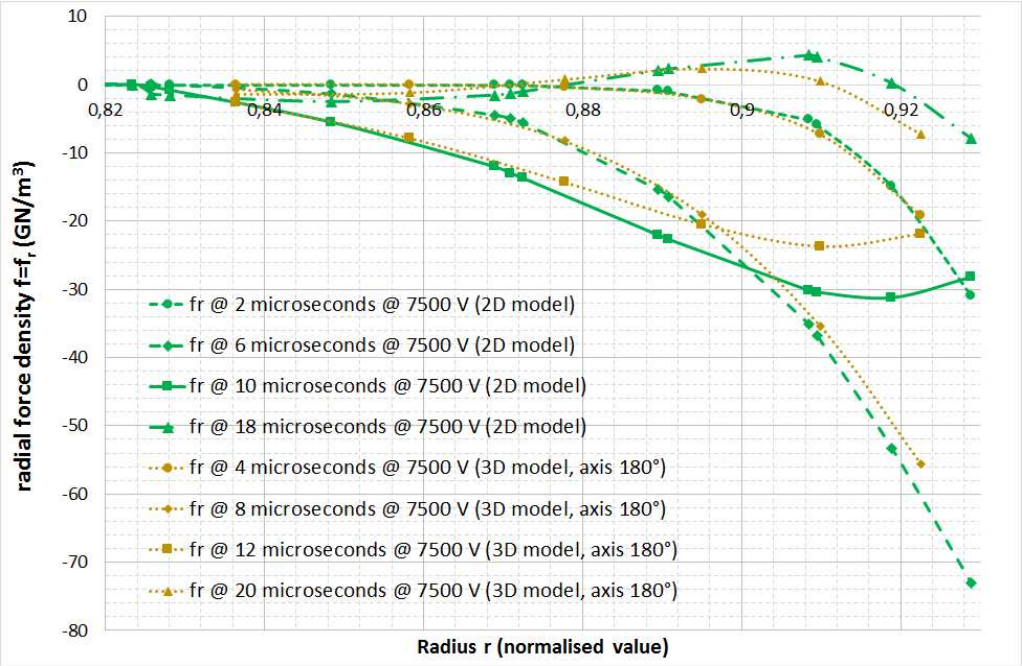

Figure 25. Transient local force density in experiment 2 (V_0 = 7500 V).

*D. Global computation results – **second experiment***

The first global results we will study are the force density on the tube surface (**Figure 26**) and the maximum absolute value of the force density inside the tube thickness (**Figure 27**). Again, peak and average values plus the natural frequency cohere to each other, whatever the model. Despite the short time delay between the 2D and the 3D model, mechanical resistance and deformation analysis are possible.

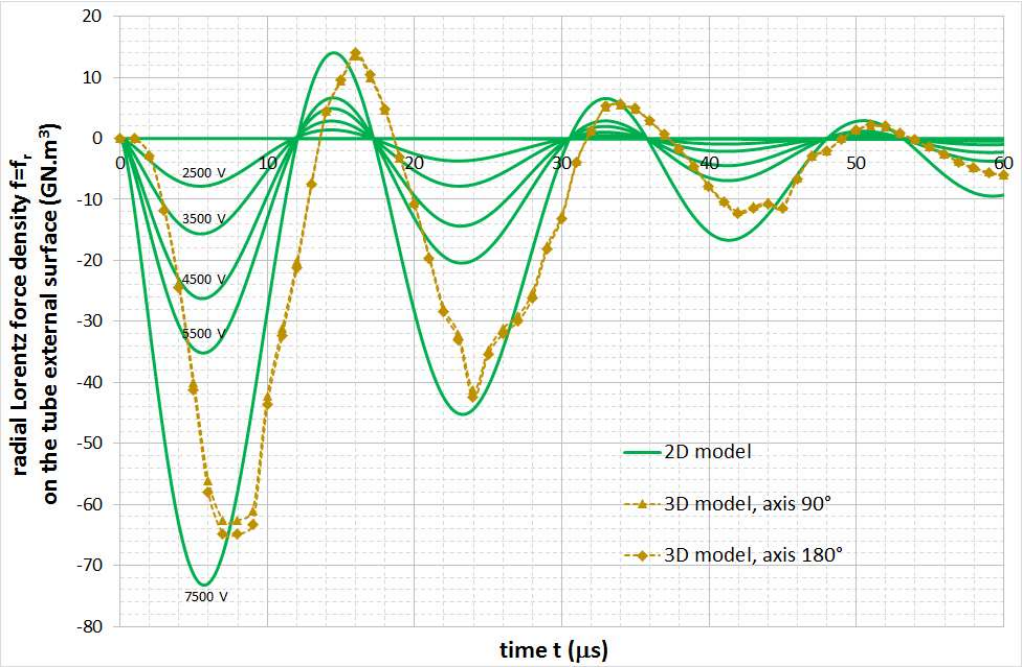

Figure 26. Force density on the tube external surface in experiment 2.

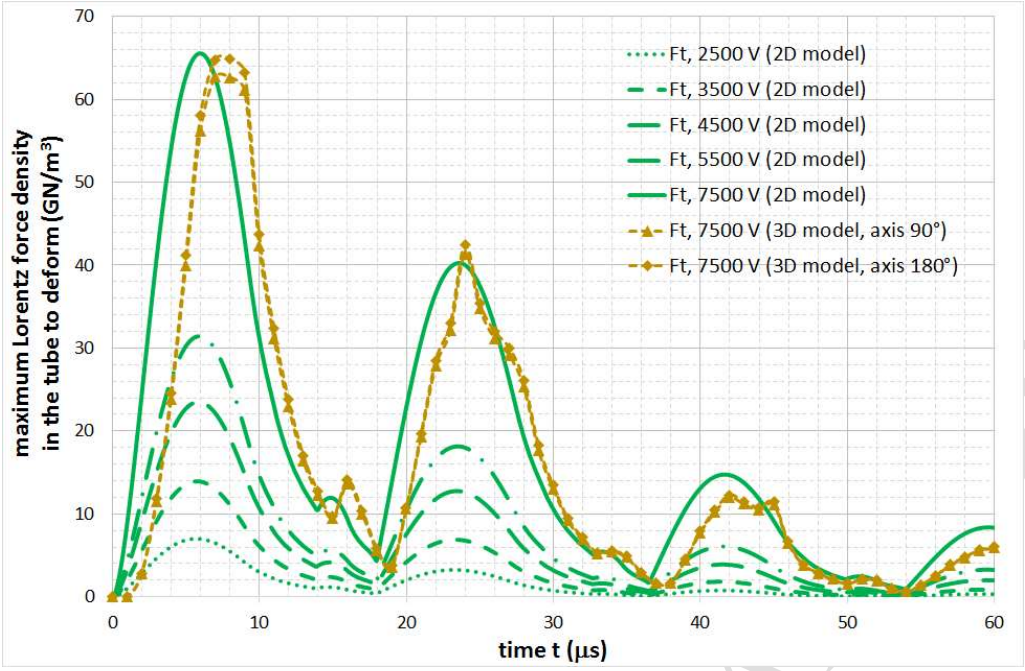

Figure 27. Maximum transient force density in the tube in experiment 2.

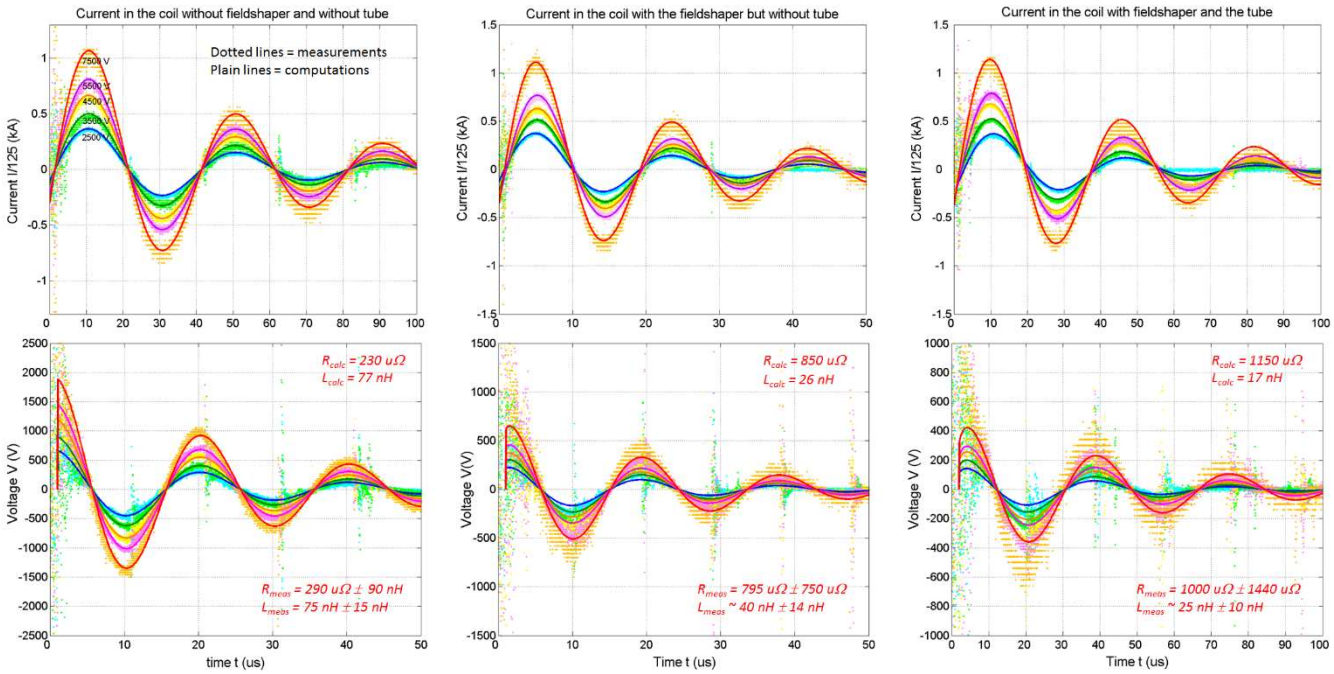

Figure 28. *I-V* curves (**a**) without field-shaper nor tube, (**b**) with field-shaper but no tube, (**c**) with field-shaper and tube (experiment 2).

E. *Experimental results – **second experiment***

Figure 28 shows the current-voltage characteristics and impedance of the coil that are measured and calculated. Electrical features of the generator are given in the Appendix A.3. The model allows the computation of the same transient pulses and of the impedance (R and L). The linear assumption is confirmed by both the measurements and the computations: R and L do not depend on the voltage magnitude. The general decaying oscillating shape of both the current and the voltage for all cases is correctly described, but still neglects high frequency disturbances, which are mainly due to the spark gaps. Peak values, natural periods and decaying factors were found in the voltage and the current pulses, giving rise to the force pulse and hence the strain.

VII. Conclusion

In this paper, we have computed the electromagnetic behavior of a single-turn toroidal coil fed by a transient current at low or medium frequency with both harmonic and transient finite element analysis.

Firstly, the main interesting coils parameters can be computed and analyzed as a function of several parameters and especially as a function of the pulse natural frequency due to the skin effect. It has been shown that the total equivalent resistance is enhanced by the presence of the tube and that it increases as a function of the frequency. The total equivalent inductance is weakened by the presence of the tube and it decreases as a function of the frequency. The coil induction coefficient is enhanced by the presence of the tube but does not depend significantly on the frequency. Finally, the induced Lorentz force should increase as a function of the frequency. It has been shown that this increase follows a root squared law that justifies the definition of original force coefficients; they consequently do not depend significantly as a function of the pulse natural frequency.

Furthermore, it has been shown that the single-turn coil with a cut can be modelled thanks to an equivalent 2D axi-symmetrical model that gives results close to the ones obtained with both a complete 3D model and experimental results. It has also been shown that the electrical circuit coupling is possible in the transient working condition, giving coherent results that are calculated imposing the transient current pulse and that are estimated in the pseudo-harmonic working conditions. A second partial conclusion is that these numerical results can be used as a mathematical reference for further analytical modeling tasks.

The transient model makes it possible to compute either the electrical behavior of the coil, with and without field-shaper or tube, or the pulsed Lorentz force and maximum force acting onto either the tube or the surface of the coil and the field-shaper. This is essential information for both the pulsed electromagnetic forming process and the study of the mechanical resistance and aging process of the coil and its materials for pulsed magnetic technologies.

Finally, the 2D model allows a vast number of calculations to be performed rendering fast and accessible any sensitivity analysis as a function of several parameters, or any coupling between several physical effects (electromagnetic, electrical, thermal, mechanical). It will thus be possible to imagine performing optimizations of the inductor concept, geometry, material or feeding and control strategy, as a function of the magnitude and duration of the pulsed magnetic field needed.

However, the present study modeled the magneto-forming process assuming the system is “fixed”. Therefore, we can only estimate if, in given conditions (*i.e.* before or after the deformation), the forming coil can ensure electromagnetic forces high enough either to initiate the process or to apply a sufficient magnetic pressure at the end of the process. Once the deformation of the workpiece begins, the complete prediction of the system behavior requires to develop a multi-physical coupling between the electromagnetic, electrical and mechanical behaviors, either with pseudo-analytical or numerical tools.

Acknowledgment

We would like to express our gratitude to the Picardie Region, the Technopole and IndustriLab who gave a financial support to this work under the project “COILTIM”.

REFERENCES

[1] R. Gersdorf, F.A. Muller, L.W. Roeland, "Design of high field magnet coils for long pulses", *JAIP Publishing, Review of Scientific Instruments*, vol. 36, pp 1100, 1965.

[2] M. N. Wilson, K. D. Srivastava, "Design of Efficient Flux Concentrators for Pulsed High Magnetic Fields", *The Review of Scientific Instruments*, August, vol. 36, Issue no. 8, 1965.

[3] V. Psyk, D. Risch, B. L. Kinsey, A. E. Tekkaya, M. Kleiner, "Electromagnetic Forming – A review", *Journal of Materials Processing Technology*, vol. 211, pp 787 – 829, 2011.

[4] D. Arnaud, J. Barbery, R. Biais, B. Fargette, P. Naudot, "Propriétés du cuivre et de ses alliages", Technique de l'Ingénieur, Article / Réf : M4640 v1, 10th of April, 1985.

[5] A. El-Azab, M. Garnich, A. Kapoor, "Modeling of the electromagnetic forming of sheet metals: state of the art and future needs", *Journal of Materials Processing Technology*, Vol. 142, pp 744 – 754, 2003.

[6] G. Bartels, W. Schätzing, H.P. Scheibe, M. Leone, "Comparison of two different simulation algorithms for the electromagnetic tube compression", *Int. J. Mater. Form.*, vol. 2, pp 693 – 696, 2009.

[7] Ph. Conraux, P. Pignol, V. Robin, J. M. Bergheau, "3D Finite Element Modeling of Electromagnetic Forming Processes", 2nd International Conference on High Speed Forming, pp. 73-82, 2006.

[8] V. Robin, E. Feulvarch, J-M. Bergheau, "Modélisation tridimensionnelle du procédé de mise en forme électromagnétique", *Mécanique et Industries*, vol. 9(2), EDP Sciences (Eds.), pp. 133-138, March-April 2008.

[9] M.A. Bahmani, K. Niayesh, A. Karimi, "3D simulation of magnetic field distribution in electromagnetic forming systems with field-shaper", *Journal of Materials Processing Technology*, vol. 209, n°5, pp. 2295 – 2301, 2009.

[10] S. Pasca, V. Fireteanu, "Transient Magnetic Finite Element Model of Magneto-forming", *Acta Electrotechnica*, vol. 45, no. 6, pp. 575-580, 2004.

[11] T. Heuzé, A. Leygue, G. Racineux, F. Chinesta, "Modélisation paramétrique d'un inducteur de magnétoformage par la Proper Generalized Decomposition", 11th colloque National en Calcul des Structures, May 2013.

[12] O. Maloberti, O. Mansouri, D. Jouaffre, D. Haye, "Harmonic and Transient Magnetic analysis of Single Turn Coils fed by a Current Pulse at Medium Frequency", COMSOL Conference, Grenoble, 14-16 october, 2015.

[13] J. Deng, C. Li, Z. Zhao, F. Tu, H. Yu, "Numerical simulation of magnetic flux and force in electromagnetic forming with attractive force", *Journal of Materials Processing Technology*, vol. 184, n°1-3, pp. 190 – 194, 2007.

[14] A. Guglielmetti, "Etude numérique du soudage par impulsion magnétique", PhD thesis, UTC Compiègne, France, 2012.

[15] D. Yanuka, S. Efimov, M. Nitishinskiv, 1. Rososhek, Ya. E. Krasik, "Generation of strong pulsed magnetic fields using a compact, short pulse generator", *Journal of Applied Physics*, vol. 119, 2016.

[16] C. V. Dodd, "A Solution to Electromagnetic Induction Problems", M. S. Thesis, University of Tennessee, Oak Ridge National Laboratory, 1967.

[17] C. V. Dodd, W. E. Deeds, "Analytical Solutions to Eddy-Current Probe-Coil Problems", *Journal of Applied Physics*, Vol. 39, pp 2829, 1968.

[18] R. Figueiredo Jardim, B. Laks, "Kelvin functions for determination of magnetic susceptibility in nonmagnetic metals", *Journal of Applied Physics*, 15 June, vol. 65, Issue no. 12, 1989.

[19] J.T. Conway, "Exact Solutions for the Magnetic Fields of Axisymmetric Solenoids and Current Distributions", *IEEE Transactions on Magnetics*, vol. 37, Issue no. 4, pp 2977 – 2988, 2001.

[20] V. Labinac, N. Erceg, D. Kotnik-Karuza, "Magnetic field of a cylindrical coil", *American Journal of Physics*, vol. 74, pp 621 – 627, 2006.

[21] D. Yu, K.S. Han, "Self-Inductance of Air-Core Circular Coils with rectangular cross section", *IEEE Transactions on Magnetics*, vol. MAG-23, Issue no. 6, pp 3916 – 3921, 1987.

[22] J.T. Conway, "Inductance calculations for nonaxial coils using Bessel functions", *IEEE Transactions on Magnetics*, Vol. 43, Issue no. 3, pp 1023 – 1034, 2007.

[23] R. Ravaud, G. Lemarquand, V. Lemarquand, S. Babic, C. Akyel, "Mutual inductance and force exerted between thick coils", *Progress in Electromagnetics Research*, vol. 102, pp 367 – 380, 2010.

[24] K. Djellabi, M.E.H. Latreche, "Induction Heating Process Design Using Comsol® Multiphysics Software Version 4.2a", World Academy of Science, *International Journal of Electrical, Computer, Electronics and Communication*, vol. 8, n°1, 2014.

[25] M. W. Kennedy, S. Akhtar, J. A. Bakken, R. E. Aune, "Analytical and Experimental Validation of Electromagnetic Simulations Using COMSOL®: Inductance, Induction Heating and Magnetic Fields", Proceedings of the 2011 COMSOL Conference in Stuttgart, 2011.

[26] O. Mansouri, O. Maloberti, D. Jouaffre, M. Hamzaoui, J. Derosière, D. Haye, J.P. Leonard, P. Pelca, "Analytical calculation of a 1-turn coil parameters for the magneto-forming technology", ICHSF Conference, Dortmund, 27-28th of April, 2016.

[27] H. A. Ghali, H. A. Rahman, "Understanding Mutual Inductance using Comsol® Multiphysics", Proceedings of the COMSOL conference, 2009.

[28] S. Babic, C. Akyel, "Improvement in Calculation of the Self- and Mutual Inductance of Thin Wall Solenoids and Disk Coils", *JIEEE Transactions on Magnetics*, vol. 36, n°4, 2000.

[29] S.A. Lockyer, F.W. Noble, "*Fatigue of precipitate strengthened Cu-Ni-Si alloy"*, Materials Science and Technology, Vol. 15, pp. 1147, 1999.

APPENDIX

A. Pseudo-Harmonic simulations

1) The coil geometry without field-shaper

***TABLE 1**: PARAMETERS OF THE COIL GEOMETRY OF TEST-CASE*

Name	Value	significance
R_{mi}	17.5 mm	internal tube radius
R_{me}	19 mm	external tube radius
g	1 mm	airgap between coil and tube
R_{ci}	20 mm	internal coil radius
R_{cie}	30 mm	intermediate coil radius
R_{ce}	100 mm	external coil radius
L_{ci}	30 mm	useful length of coil
L_{ce}	50 mm	total length of coil

2) The materials

***TABLE 2**: PARAMETERS OF THE MATERIALS (@20°C) OF TEST-CASE*

Name	Value	significance
σ_m	75 % IACS*	Tube electrical conductivity
μ_m	μ_0	Tube magnetic permeability
σ_c	10 % IACS*	Coil electrical conductivity
μ_c	μ_0	Coil magnetic permeability

*IACS: International Annealed Copper Standard (100 % = σ_{Cu})

3) Other electrical parameters

Frequency: *f = 20 kHz* / Peak current: *I = 825*Z[mm]/30 kA*

B. Transient and first experiment

1) The coil geometry without field-shaper

***TABLE 3**: PARAMETERS OF THE COIL GEOMETRY OF EXPERIMENT 1*

Name	Value*	significance
R_{mi}	0.876	internal tube radius
R_{me}	0.942	external tube radius
$g=g_{mc}$	0.0578	airgap between coil and tube
R_{ci}	1	internal coil radius
R_{cie}	1.98	intermediate coil radius
R_{ce}	6.6	external coil radius
L_{ci}	1.98	useful length of coil
L_{ce}	3.3	total length of coil

*Values normalized as a function of reference value R_{ci}=1.

2) The materials

***TABLE 4**: PARAMETERS OF THE MATERIALS (@20°C) OF EXPERIMENT 1*

Name	Value	significance
σ_m	30-70 % IACS*	Tube electrical conductivity (weak impact on I-V results)
μ_m	μ_0	Tube magnetic permeability
σ_c	7 % IACS*	Coil electrical conductivity
μ_c	μ_0	Coil magnetic permeability

3) Other electrical parameters

I_{peak}=175.6 kA, τ=41.7 µs, f_q = 27.5 kHz (with a tube)

C. Second experiment with field-shaper

1) The coil and field-shaper geometry

***TABLE 5**: PARAMETERS OF THE COIL GEOMETRY OF EXPERIMENT 2*

Name	Value*	significance
R_{mi}	0.823	internal tube radius
R_{me}	0.926	external tube radius
$g=g_{mf}$	0.0742	airgap between coil and tube
R_{fi}	1	internal field-shaper radius
R_{fie}	2.292	mid field-shaper radius
R_{fe}	3.292	external field-shaper radius
g_{fc}	0.042	airgap field-shaper - coil
R_{ci}	3.333	internal coil radius
R_{ce}	6.583	external coil radius
L_{fi}	1.25	useful length of field-shaper
L_{fe}	2.5	total length of coil

*Values normalised as a function of reference value R_{fi}=1.

2) The materials

***TABLE 6**: PARAMETERS OF MATERIALS (@20°C) OF EXPERIMENT 2*

Name	Value	significance
σ_m	30 % IACS*	Tube electrical conductivity
μ_m	μ_0	Tube magnetic permeability
σ_f	46 % IACS*	Field-shaper conductivity
μ_f	μ_0	Field-shaper permeability
σ_c	46 % IACS*	Coil electrical conductivity
μ_c	μ_0	Coil magnetic permeability

3) Other electrical parameters

Initial capacitor voltage: *V_0 = 0-8500 V*; Generator capacitance: *C = 138 µF / module*; Generator and cables resistance: *R_1 = 12 mΩ / module*; Generator and cables inductance: *L_1 = 220 nH / module.*